"Beyond Weather Regimes": Descriptors Monitoring Atmospheric Centers of Action. A case study for Aotearoa New Zealand

Benjamin Pohl, Andrew Lorrey, Andrew Sturman, Hervé Quénol, James Renwick, Nicolas Fauchereau, Julien Pergaud

“Beyond Weather Regimes”: Descriptors Monitoring Atmospheric Centers of Action. A case study for Aotearoa New Zealand

Benjamin Pohl[1]*; Andrew Lorrey[2]; Andrew Sturman[3]; Hervé Quénol[4]; James Renwick[5]; Nicolas Fauchereau[2]; Julien Pergaud[1]

[1] Biogéosciences, UMR6282 CNRS / Université de Bourgogne Franche-Comté, Dijon, France
[2] National Institute of Water and Atmospheric Research, Auckland, New Zealand
[3] School of Earth and Environment, University of Canterbury, Christchurch, New Zealand
[4] UMR6554 LETG CNRS, Université Rennes 2, Rennes, France
5 School of Geography, Environment & Earth Sciences, Victoria University of Wellington, Wellington, New Zealand

Submitted to
Journal of Climate
2 February 2021
Revised
15 June 2021
20 July 2021
Accepted
23 July 2021

*** Corresponding Author Address**
Benjamin Pohl — Laboratoire Biogéosciences
6 bvd. Gabriel — 21000 Dijon — FRANCE
(+33)380393821 | benjamin.pohl@u-bourgogne.fr

Abstract

This paper introduces a set of descriptors applied to weather regimes, that allow for a detailed monitoring of the location and intensity of their atmospheric centers of action (e.g. troughs and ridges) and the gradients between them, when applicable. Descriptors are designed to document the effect of climate variability and change in modulating the character of daily weather regimes, rather than merely their occurrence statistics.

As a case study, the methodology is applied to Aotearoa New Zealand (ANZ), using ERA5 ensemble reanalysis data for the period 1979-2019. Here, we analyze teleconnections between the regimes and their descriptors, and large-scale climate variability. Results show a significant modulation of centers of action by the phase of the Southern Annular Mode, with a strong relationship identified with the latitude of atmospheric ridges. Significant associations with El Niño Southern Oscillation are also identified. Modes of large-scale variability have a stronger influence on the regimes' intrinsic features than their occurrence. This demonstrates the usefulness of such descriptors, which help understand the relationship between mid-latitude transient perturbations and large-scale modes of climate variability.

In future research, this methodological framework will be applied to analyze (i) low-frequency changes in weather regimes under climate change, in line with the southward shift of storm tracks, and (ii) regional-scale effects on the climate of ANZ, resulting from interaction with its topography.

Keywords

weather regimes — synoptic variability — southern midlatitudes — teleconnections — Southern Annular Mode — Aotearoa New Zealand

"Beyond Weather Regimes": Descriptors Monitoring Atmospheric Centers of Action. A case study for Aotearoa New Zealand

1. Introduction

Analysis of weather regimes (WRs) is commonly used to investigate climate variability across time and spatial scales (Straus et al. 2007; Richard et al. 2018; Moron et al. 2015, 2019, 2018; Vrac et al. 2014). It has been widely and successfully used to cluster high-frequency (daily or sub-daily) atmospheric fields (e.g., using geopotential height: Cassou *et al.*, 2004, 2005; Cassou, 2008), or climate variables (such as a proxy of atmospheric convection: Fauchereau *et al.*, 2009; Vigaud *et al.*, 2012; Vigaud and Robertson, 2017), into a limited number of recurrent patterns. The time distribution of WRs can then be used to analyze low-frequency (interannual, decadal, centennial, multi-centennial; e.g., Lorrey et al. 2007; Pohl and Fauchereau 2012; Vrac et al. 2014; Pohl et al. 2018) mean climate state conditions. Weather regimes are often obtained using semi-automatic multivariate clustering algorithms, typically after an empirical orthogonal function (EOF) analysis that reduces the dimensionality of the dataset to be classified. Classification or clustering techniques can either be hierarchical (Crétat et al. 2012; Cheng and Wallace 1993) or non-hierarchical (Michelangeli et al. 1995; Huth 1996). Among the latter category, the k-means algorithm (Moron and Plaut 2003; Vautard 1990; Michelangeli et al. 1995) and the self-organizing maps technique (SOMs: Hewitson and Crane 2002; Gibson et al. 2017; Sheridan and Lee 2011) are the most commonly used in climate sciences.

Although there has been some controversy about the existence (Stephenson et al. 2004) or number (Christiansen 2007) of WRs identified, the main limitations of this technique are that:

(i) it ignores the continuous nature of climate variability and expresses synoptic variability as a limited number of discrete atmospheric configurations; and (ii) it drastically simplifies variability and acts as a spatio-temporal filter that only retains the main features of the regional circulation associated with the largest variance. These shortcomings illustrate that a limited number of recurrent patterns cannot capture the full diversity and complexity of spatiotemporal variability, and raises the question of the ability of WR categorizations to account for changes that are associated with lower variance. This may reduce the relevance and usefulness of clustering for documenting slowly-changing climate conditions, like (multi-)decadal variability or longer term climate change projections, with most of the variance of the input fields often originating from synoptic or intraseasonal transient perturbations (Champagne et al. 2019).

Hence, the behavior of WRs when applied to long time periods can be uncertain. Over the Pacific – North American region, Straus *et al.* (2007) found that their circulation regimes had some skill for characterizing interannual variability, while Lorrey and Fauchereau (2017) reached similar conclusions over the southwest Pacific region. In the Arctic, Champagne *et al.* (2019) stated that changes in the frequency of WRs typically explain between 15-20 and 40% of the year-to-year climate variability, as well as differential warming rates between subregions. Over Southern Africa, Fauchereau *et al.* (2009) established significant relationships between convective regimes, discriminating patterns of large-scale atmospheric convection and interannual climate variability. Pohl *et al.* (2018) extended these results to the quasi- and multi-decadal timescales and found that both regime frequencies and their intrinsic properties act to shape low-frequency climate fluctuations. A similar result was obtained at the scale of the whole Southern Hemisphere by Pohl and Fauchereau (2012), who attempted to decompose the multi-decadal shift towards the positive phase of the Southern Annular Mode (Thompson et al. 2011; Marshall 2003; Renwick 2004) into WRs. They pointed out that roughly half of the long-

term change in the SAM relates to regime frequency, while the other half is related to changes in their internal characteristics. At the more regional scale of Aotearoa New Zealand (ANZ), Lorrey et al. (2007) investigated Kidson's (2000) synoptic types and their relationship to regional rainfall guided by the Interdecadal Pacific Oscillation, although that analysis was notably constrained to only one multidecadal cycle. Parsons *et al.* (2014) used the same WRs to evaluate climate model outputs and analyzed climate change projections regionally. Surprisingly, in spite of the well documented southward shift expected in the mid-latitude storm track (under the combined influence of stratospheric ozone and increasing concentrations of greenhouse gas concentrations: Fogt *et al.*, 2009; Perlwitz, 2011; Polvani *et al.*, 2011; Zheng *et al.*, 2013), this study found only a very weak sensitivity of synoptic WRs to climate change, even for the latter part of the 21st century and under high-emission scenarios.

Changes occurring within the regimes are thus a key feature to be considered, because a major, if not dominant, part of the variance is associated with them. Another reason is that WRs are often used as analogues (Ouzeau et al. 2011; Ullmann et al. 2013; Michaelides et al. 2007) to investigate perturbations (e.g. in precipitation or temperature) linked to climate change under similar atmospheric configurations – hence the need to separate changes in the WRs themselves from time-transgressive anomalies occurring under stationary regimes. In spite of the importance of this issue, both for impact studies and for a more detailed understanding of atmospheric dynamics, this has been rather neglected to date. A possible explanation is that most previous work explicitly analyzed regime occurrence and temporal variability, and did not propose internal descriptors to monitor within-regime changes.

This study addresses this knowledge gap by targeting the ANZ region of the southwest Pacific as a case study representative of southern mid-latitudes. We propose here a set of atmospheric

descriptors internal to pre-existing WRs (Kidson 2000; Jiang et al. 2004, 2013a; Fauchereau et al. 2016; Renwick 2011) that allow simple monitoring of their main atmospheric centers of action (e.g. associated pressure anomaly extremes; e.g., Osman *et al.*, 2020), and their physical properties (i.e., the location and intensity). This allows for a more detailed assessment of their variability in space and time, and their effects and impacts on regional climate at a wide range of timescales, spanning short-term/high-frequency fluctuations of weather to low-frequency variability, either driven by natural dynamics or anthropogenic forcings.

The present study focuses on the reanalysis dependency of WRs and their internal descriptors, and assesses the large-scale background conditions that drive WR frequency and fluctuations in their descriptors. Future work will be dedicated to seamless analysis of the impacts of climate variability and change, using the same approach of monitoring atmospheric centers of action at various temporal and spatial scales. This question is of crucial importance in the Southern Hemisphere, in line with the low-frequency circulation changes discussed above.

Section 2 presents the datasets and the methods used to monitor and analyze the atmospheric centers of action associated with the WRs described by Kidson (2000). Section 3 presents the reanalysis dependency of the results, by comparing the original distribution of WRs obtained with NCEP/NCAR with those of the more recent ERA5 reanalysis. Section 4 discusses the large-scale climate conditions and the teleconnections that modulate these centers of action and their intrinsic properties. Section 5 summarizes the main results and provides concluding remarks.

2. Data and Methods

2.1 Data

Atmospheric fields used in this study are taken from the ERA5 ensemble reanalysis (Hersbach et al. 2020). ERA5 is the fifth generation of atmospheric reanalysis released by the European Centre for Medium-Range Weather Forecasts. It currently covers the period 1979 onwards (with planned extension to 1950 onwards) and includes a 10-member ensemble to quantify uncertainties associated with the density and quality of the assimilated data. In this work, we use the regular 0.5° x 0.5° grids of the ensemble for daily mean fields of geopotential height at 1000 (Z1000) and 700 hPa (Z700) over the period 1979-2019.

Global sea surface temperature (SST) fields (°C) are taken from the ERSST v5 database (Huang et al. 2017), available at a monthly time step on a 2° x 2° global grid. This product, suited for long-term and large-scale studies, is used here to analyze global teleconnections with our weather regimes. It offers robust estimations of basin-wide or global patterns, but smooths local and coastal features.

A daily Southern Annular Mode (SAM) index is used to assess relationships between the WRs and the state of the climate in the Southern Hemisphere. The observation-based index of Marshall (2003) is selected, since it avoids spurious trends often found in reanalysis-based SAM indices. This index is available since 1957 and computed as the mean atmospheric pressure difference between “high-latitudes” (stations located between 50°S and 70°S) and “mid-latitudes” (stations between 30°S and 50°S).

The state of El Niño Southern Oscillation (ENSO) is monitored by a regional SST index averaged spatially over the Niño3.4 region (5°N-5°S, 170°W-120°W). Here, we chose the most commonly-used index, derived from the HadlSST database (Rayner et al. 2003) and available since 1870 with a monthly timestep.

2.2 Weather regime redefinition using the ERA5 ensemble

Original WRs as defined by Kidson (2000) are based on a k-means clustering (Cheng and Wallace 1993) of 12-hourly maps of Z1000 derived from NCEP/NCAR reanalyses (Kalnay et al. 1996) into 12 types. We chose here not to include NCEP/NCAR spatial fields of Z1000 in this study in order to perform a new analysis of these WRs, since more recent generations of reanalyses, using updated models and better assimilation techniques, are now available to provide atmospheric fields of better quality. This issue is of major importance in the Southern Hemisphere, where the density of assimilated data is much less than in northern mid-latitudes. Another reason is that NCEP/NCAR reanalyses are provided at a 2.5° x 2.5° resolution, which is more coarse and less able to define precise coordinates of atmospheric centers of action.

Using newer reanalyses (namely, ERA5) requires redefining the original WRs onto grids of a different resolution and time period. To do so, we proceeded as follows:

— 1. we used the original time distribution of WRs (defined with NCEP/NCAR) to compute the composite mean Z1000 raw and anomaly fields associated with the 12 WRs in ERA5 (Fig. 1, inner domain). Z1000 patterns based on ERA5 are remarkably similar to those found in the literature and based on NCEP/NCAR (Kidson, 2000; Jiang *et al.*, 2004; Jiang, 2011; Renwick, 2011; Parsons *et al.*, 2014; Fauchereau *et al.*, 2016, among others). This denotes, at first order, general agreement across reanalyses.

— 2. The mean composite maps of Z1000 (Fig. 1) were then used to re-ascribe each day of each member of the ERA5 ensemble to the nearest attractor, by minimizing the Euclidean distance *d* between each daily field and the 12 Z1000 patterns associated with the WRs.

To match the methodology used by Kidson (2000) to obtain the WRs, a preliminary EOF analysis was performed to filter out atmospheric noise and reduce the amount of data. As in Kidson (2000), five principal components (explaining 94.7% of the original variance of the Z1000 field) were retained. Thus, in the second step above, these are the scores of each day of each member that were used, together with the mean score of each attractor, to compute *d* and affiliate each day to the attractor minimizing *d*.

This implies that two distinct time distributions of the 12 WRs are available: one based on (and referred to hereafter as) the original NCEP/NCAR timing, and one based on the redefinition of each day of each member of ERA5 to the nearest attractor (hence referred to as the ERA5 redefinition). These two categorizations are further discussed and compared below. Even though one of the time distributions is inherited from the NCEP/NCAR reanalysis, all analyses performed in this work are based on ERA5 data, thought to be more precise and probably more realistic.

2.3 Definition of internal descriptors monitoring centers of action

Kidson (2000) and subsequent studies separated the 12 WRs into three groups of regimes called trough, zonal and blocking. They merely presented raw Z1000 fields near ANZ and did not consider Z1000 anomalies (noted Z1000' hereafter). Here, we propose a slightly different approach that allows us to define internal descriptors within each WR, in order to monitor associated centers of action (Fig. 1):

- First, after removing the mean (unsmoothed) annual cycle, Z1000' are considered instead of Z1000 raw composites. Anomalies are preferred here because the synoptic centers of action are easier to detect, locate, and quantify (in terms of intensity), than when considering the raw fields.
- Next, the domain is enlarged to match the typical size of mid-latitude transient perturbations, and to include the regional extremes of Z1000' (Fig. 1). The choice of the domain size is of major importance, because a domain that is too small would lead to underestimation of the range of possible locations for the centers of action, hereby reducing their spatial variability. Alternatively, too large a domain could lead to the extraction of regional extremes of Z1000' that relate to other features located at the periphery of the domain, but are not directly related to the WRs themselves. The domain used here is 20°S – 65°S, 140°E – 210°E. It was found to be the best compromise for all 12 WRs, allowing for a simple monitoring of their centers of action, without extra parameterization to constrain the extraction of Z1000' extremes within a prescribed subdomain (that could potentially be different for each WR). Overall, choosing a convenient domain for all WRs keeps the method simple and straightforward.
- Last, three new groups of regimes are formed, which do not correspond to those of Kidson (2000). These groups are defined depending on the presence or absence of regional extremes of Z1000' (Fig. 1, Table 1). The “Low” group has only one such extreme, consisting of a regional minimum of Z1000' denoting an atmospheric trough. Symmetrically, the “High” group only includes a regional maximum of Z1000', indicative of an atmospheric ridge. The “Gradient” group has both extremes. The internal descriptors introduced in this work are group-dependent. For the “Low” regimes, three metrics are defined: the intensity of the low, corresponding to the minimum Z1000' value within the whole domain ($Min_{Z'}$), and its corresponding latitude

and longitude (*Lat*, *Lon*) defining its location (Table 1). The "High" types use the same metrics, but applied to the extracted Z1000' maximum. The "Gradient" types mix both metrics (Table 1), and add new ones that monitor the relative position and differences between both extremes. This provides the difference between Z1000' maximum and minimum ($Diff_{Z'}$), the latitudinal and longitudinal differences in their locations ($Diff_{Lat}$, $Diff_{Lon}$), and finally the slope of the geopotential height gradient, defined as $Grad = Diff_{Z'}/\sqrt{Diff_{Lat}^2 + Diff_{Lon}^2}$.

3. Reanalysis dependency of weather regimes and their centers of action

Here, we redefine the time distribution of regimes using ERA5 ensemble reanalysis and assess the variability, in both time and space, of the atmospheric centers of action associated with these regimes.

3.1 Time distribution and reproducibility

Figure 2 shows the (dis)agreement between both the original NCEP/NCAR time distribution of the 12 WRs and their redefinition in the ERA5 ensemble (upper panel), associated reproducibility (i.e. inter-member agreement: middle panel), and the time distribution of the WRs according to ERA5 (lower panel). A first striking result is the large number of days showing disagreement between the two reanalyses: 33% of the days of the period are ascribed to a different WR according to the original and redefined classifications (Fig. 2, upper panel). These differences result in WR frequencies that can sensibly differ across reanalyses (Table 2), especially for regimes SW (1774 days according to NCEP/NCAR against 1281 in ERA5), H

(2105 vs. 1580 days) or W (830 vs. 1294 days). Detailed analysis reveals that most permutations between WRs concern patterns are quite close, and that mostly differ in the location of similar centers of action (Table 2). For example, days ascribed to regime T in ERA5 are often ascribed to regime SW in NCEP/NCAR, with these regimes both consisting of a trough located slightly more to the southeast in SW (Fig. 1). All the main disagreements in Table 2 concern regimes that are quite similar, physically (e.g. the H regime resembling both HNW and HSE or, to a lesser extent, HE and HW; or the T regime that recurrently swaps with SW, TNW and TSW). Statistically, these permutations correspond to days almost equidistant from two cluster centroids.

The cumulative effect of these disagreements is shown in Supp. Fig. 1. Generally speaking, the centers of action tend to be slightly stronger when regimes are redefined in ERA5, i.e. larger negative Z1000' associated with troughs (T, SW, TSW) and more positive Z1000' with ridges (H, W, HSE). Yet, there are also day swaps between regimes that act to weaken the synoptic configurations (a weaker trough for TNW and weaker ridge for HNW and HE). Supp Fig. 2 shows that differences between reanalyses do not strongly modify the seasonal distribution of the WRs, even if the seasonal peak of some regimes may be damped (e.g. SW) or enhanced (e.g. HW) in ERA5 redefinitions compared to the original NCEP/NCAR timing. Supp. Fig. 3 further shows that the interannual variability of the regimes is consistent across reanalyses. Considering seasonal WR occurrences in austral summer (November through February, NDJF), interannual correlations range between 0.59 (HNW) and 0.93 (HSE). In austral winter (June through September, JJAS), these values span from 0.70 (TNW) to 0.88 (T and TSW).

These disagreements between reanalyses are much larger than the uncertainties within the ERA5 ensemble (Fig. 2, middle panel). The latter seem to be even slightly decreasing in recent

years, mostly since 2001. Over the whole period, 96.7% of the days are associated with the same WR for all 10 members in ERA5 (indicative of perfectly reproducible regime attribution), a value that increases from 95.8% to 97.9% before and after 2001. When reanalyses disagree, their differences tend to be highly reproducible across ensemble members: only 2.4% of the days show partial, member-dependent agreement across reanalyses. This suggests a strong observational constraint on reanalyzed fields, suggesting that the amount and quality of data assimilated do not represent a limiting factor that could partly explain such differences between reanalyses. We can, however, hypothesize that part of these differences may relate to the numerical models, or their assimilation schemes. It is also clear that they relate to the resolution jump between NCEP/NCAR and ERA5 (0.5° for the 10-member ensemble or 0.25° for the unperturbed member in ERA5, against 2.5° for the deterministic NCEP/NCAR member). Such coarse resolution in NCEP/NCAR could explain why regimes differing by small changes in the location of their centers of action are associated with the largest differences across WRs. Increased resolution allows for a much more precise characterization of the location and intensity of the main centers of action.

Since we cannot consider the reanalysis dependency of WR time distribution to be negligible, all analyses presented below have been duplicated for both the original and redefined time distributions. None of the conclusions obtained here have been qualitatively modified when changing WR classifications (not shown), and only scientific results obtained with both time distributions are presented and discussed below, in order to ensure statistical and physical robustness.

3.2 Daily variability in atmospheric centers of action

Synoptic WRs defined by Kidson (2000) have been used for paleoclimate reconstructions in the Holocene (Lorrey et al. 2007, 2008; Ackerley et al. 2011; Lorrey et al. 2012, 2014) and Little Ice Age (Lorrey et al. 2014), and to analyze climate change projections (Parsons et al. 2014). Significant relationships have been established between these WRs and the Madden-Julian Oscillation (Fauchereau et al. 2016), the Interdecadal Pacific Oscillation (Lorrey et al. 2007) and the Southern Hemisphere large-scale background conditions (Renwick 2011). Using similar regimes, Jiang *et al.* (2004) and Lorrey and Fauchereau (2017) also found significant relationships with ENSO. At the more local and regional scales, Kidson types have been shown to drive daily climate anomalies (Kidson 2000; Renwick 2011), seasonal rainfall anomalies (Lorrey et al. 2007) and air quality (Appelhans et al. 2013) over ANZ, and modulate ocean wave heights (Coggins et al. 2016) and ocean-atmosphere coupled summer heatwaves (Salinger et al. 2020). Yet, in spite of their relevance for analyzing climate variability in the ANZ sector, none of the previous work considered the internal variability and diversity within these WRs, and solely focused on WR occurrence. This remark remains true for most studies based on WRs, including those proposing long-term reconstruction over the past decades (e.g., Ackerley et al. 2011; Pohl et al. 2018) and climate change projections by the end of the current century (e.g., Vrac et al. 2014). The descriptors defined in this work may help address this issue. In order to illustrate their usefulness, Figure 3 presents the case of the TNW regime (all other regimes and their associated descriptors can be found in Supp. Figs. 7 to 17). TNW is chosen here as an example because it shows particularly strong co-variability with modes of large-scale variability at both tropical and polar latitudes (see below). It is a Gradient-type regime that occurs on 1042 days during the period 1979-2019 (Table 2). It is characterized by a Z1000' minimum located west of the South Island of ANZ, and a Z1000' maximum to the southeast. This dipole, with a trough situated northwest of a ridge, results in a strong northwesterly mean flow that is frequently associated with a local pressure field perturbed by the Southern Alps

running along the backbone of the South Island of ANZ, as indicated by the Z1000 isolines (Fig. 3).

For each of the 10 descriptors associated with the "Gradient" types (Table 1), we extracted the 20% lowest and 20% highest values (i.e. we considered the opposite phases of each descriptor using the 20th and 80th percentiles) and plotted corresponding Z1000 and Z1000' composite means (Fig. 3). Each map corresponds to the average of 208 days, that is, 20% of the total TNW regime over the period. Very similar results have been obtained when extracting the 5, 10, 15 or 25th percentiles of both polarities (not shown); moreover, the overlap between these samples (the opposite phases of each descriptor) is shown and discussed in the Supplementary Materials. The maps of Figure 3 show day-to-day diversity usually concealed in the overall mean pattern within TNW occurrences. A first general statement is that the Z1000' dipole is present in all subsamples associated with the opposite phases of the descriptors, which denotes some qualitative stability in the anomaly pattern within this regime. However, quantitative differences between the subsamples are obvious when examining the patterns in more detail. They show a spatial dislocation of Z1000' extreme values, as well as a difference in Z1000' amplitudes. For instance, the 20% lowest (highest) Z1000' minimum values associated with the trough located west of ANZ ($Min_{Z'}$) are roughly -130 m (-70 m), and contrasts are even larger variability for the atmospheric ridge situated in the southeastern part of the domain ($Max_{Z'}$, with 20th and 80th percentiles values at +40 and +180 m, respectively). These metrics strongly control the disturbances of the regional pressure field and the sinuosity of westerly wind fluxes (the most exaggerated ones being reminiscent of small cut-off lows: e.g., for *LonMax*–), and thus, the atmospheric circulation over the whole region. Regional consequences for the climate of ANZ will be considered in future work.

Figure 4 generalizes this analysis for all WRs, and shows the statistical distribution for the 12 WR descriptors according to the respective ERA5 ensemble mean. Associated uncertainties within the ensemble (i.e., inter-member standard deviation of each descriptor) are shown in Supp. Fig. 4. The negative centers of action ($Min_{Z'}$, that is, the intensity of the troughs for both "Low" and "Gradient" regimes) are logically characterized by negative Z1000', with median values ranging between -220 m (SW) and -170 m (HE and R). Daily instantaneous values vary across a much wider range, from -40 m (HW) to -415 m (SW). The boxplots show large variability from one day to another, which is concealed when evaluating only WR mean properties. The inter-quartile range is quite similar from one regime to another, suggesting that all regimes display internal variability of comparable magnitude. Qualitatively similar results concern the positive centers of action ($Max_{Z'}$, monitoring atmospheric ridges of "High" and "Gradient"), albeit with slightly weaker but positive values. Regimes HNW and W (HSE, HE and TNW) are associated with the weakest (strongest) Z1000'. Geopotential height differences between the centers of action of "Gradient" regimes are slightly larger for regimes TNW and HNW and weaker for R, yet the magnitude of day-to-day variability of this descriptor ($Diff_{Z'}$) is quite similar across WRs. Inter-member uncertainties are very weak when compared to the amplitude of anomalies (Supp. Fig. 4), being typically ±2 m for $Min_{Z'}$, ±1 m for $Max_{Z'}$ and ±3 m for $Diff_{Z'}$, compared to values of ~ -200 m, +150 m and 300-350 m, respectively.

The spatial coordinates of the centers of action appear much more variable both across WRs, and across days associated with each WR (Fig. 4). For these descriptors, the choice of the domain is of crucial importance in order to monitor the whole range of possible locations, while excluding anomaly patterns around the WRs, but not directly related to them. The extreme values of latitudes and longitudes are bounded by the location of the domain boundaries, but this limitation only concerns a few days since most of the distribution does not reach the domain

limits. The location of the troughs (*LatMin*, *LonMin*) is generally more variable than the ridges (*LatMax*, *LonMax*), especially for regimes HE and R. Exceptions are: (i) regimes SW and to a lesser extent HNW (the trough location being weakly variable from one day to another), and (ii) regimes HNW and W (ridges being more variable spatially than for all other WRs: Fig. 4). The longitudinal and latitudinal distances that separate the two centers of action of the "Gradient" regimes (*DiffLat*, *DiffLon*) are more constant than their absolute location, which could be due to the fact that they reflect the zonal and meridional size and extension of temperate transient perturbations, like atmospheric Rossby waves, and are thus constrained by the physical properties (i.e. the wavelength) of the latter. Associated inter-member uncertainties are very weak (Supp. Fig. 4), with median and mean values weaker than the grid resolution (0.5°). Finally, geopotential gradient (*Grad.*) is also quite comparable across "Gradient" regimes, although TNW, HE and R tend to show larger values. Once again, corresponding uncertainties are low (Supp. Fig. 4). These results indicate that the deterministic members derived from ERA5 could give robust results when characterizing the spatio-temporal features of the main synoptic centers of action associated with the KTs, at least since 1979.

3.3 Seasonality and seasonal persistence

We examined "High" regimes in order to explore descriptor seasonality (see Supplementary Figure 5), with a focus on how centers of action, intensity and location are modified through the year. Qualitatively similar results hold for all three groups of WRs (not shown). Z1000' tends to show larger absolute values in winter, but their location (latitude and longitude) is stationary throughout the year (Supp. Fig. 5). Analysis of all WRs and associated descriptors only for the summer or winter season (Supp. Figs. 7-17) reveals that the amplitude of Z1000' anomalies is the only feature that changes, while patterns remain similar in all other aspects

(not shown). This illustrates how the general circulation, stronger in winter, affects regional-scale WRs.

Figure 5 addresses the question of the variability in timescales of the descriptors, using once again the example of the TNW regime (Fig. 3) in winter. Qualitatively similar results hold for all WRs, and are also verified for the summer season (not shown). We assessed if atmospheric centers of action, previously identified as highly variable in location and intensity (Fig. 4), show some seasonal persistence, or marked inter-event differences (i.e., differing properties for successive WR days or sequences occurring within the same season). Some winter seasons display a very large spread in WR descriptors, indicative of properties that strongly differ between sequences, or days ascribed to the considered WR. In other cases, however, descriptors show strong consistency during a given season, with very weak variability from one day or sequence to another (Fig. 5). The magnitude of intraseasonal variability is statistically independent from the seasonal mean value of the descriptor. A given descriptor is as likely to exhibit a weak or a strong spread whatever its average value, including strongly positive or negative seasonal means. This suggests that, at least during given seasons, some mechanisms or seasonal background conditions could be responsible for both seasonal departure and seasonal persistence of anomalous descriptor values. This leads us to investigate, in Section 4, the relationships between WR descriptors and modes of large-scale climate variability at the daily and seasonal timescales.

This section has shown that atmospheric centers of action associated with WRs exhibit large variability, either in their spatial coordinates or their intensities. This accounts for the strong residual diversity that remains within days ascribed to the same regime.

475

4. Large-scale control on synoptic centers of action

In this section, we analyze long-term trends in the atmospheric centers of action, as inferred by our descriptors, over the last four decades (since 1979), and their relationships with the main
480 modes of climate variability shown in the literature to modulate the weather types in the ANZ sector, namely, ENSO and the SAM.

4.1 Low-frequency trends

485 The southward shift of the storm track and westerly winds in the Southern Hemisphere that occurred during the 20th century (Jones et al. 2009; Fogt et al. 2009; Polvani et al. 2011) should lead to changes in mid-latitude WRs as represented by Kidson types. Such low-frequency changes have so far merely been addressed in terms of regime occurrence, ignoring internal changes in WR characteristics. Here, even though the period covered (since 1979) may be too
490 short to extract robust low-frequency trends and changes (Lorrey *et al.*, 2007 identified, for instance, the mid-1970s as a turning period for climate variability in the ANZ region, a result confirmed by Favier *et al.*, 2016 for the mid-latitudes of the South Indian sector), we test the stationarity not only of WR occurrence, but also of their characteristics as represented by the descriptors (Figs. 6-7 for the austral winter and summer seasons, respectively).

495

For both seasons, none of the WR frequencies show a significant long-term trend, either positive or negative, since 1979 (Figs. 6-7). This result is verified using both regime distributions (derived from NCEP/NCAR and ERA5). Only a few descriptors reach statistical significance in recent decades in terms of long-term change, particularly in the summer season

when the T regime seems to be associated with more intense troughs ($Min_{Z'}$) located at increasing longitudes (Fig. 7). TNW shows a similar evolution for the intensity of associated low-pressure centers of action, while HNW shows an intensification of highs. Regime SW is the only regime that shows low-frequency changes in the latitude of its atmospheric lows. In winter (Fig. 6), the main low-frequency changes concern the latitude of the atmospheric ridges associated with regimes W, HSE and NE, with a positive (northward) trend in their latitude that could result from a southward shift of transient perturbations. This latitudinal shift promotes increased stability at subtropical latitudes, consistent with a poleward expansion of the Hadley circulation (e.g., Lu *et al.*, 2007; Hu *et al.*, 2011; Tao *et al.*, 2016; Nguyen *et al.*, 2018). Yet, caution is needed here, since the recent time period is not optimal for such trend analysis. In the following we further investigate the factors (large-scale modes and background climate conditions) that drive the location and intensity of atmospheric centers of action.

4.2 Teleconnection with ENSO

Using the updated classification of Jiang (2011), Jiang *et al.* (2004, 2013b) analyzed the relationship between ENSO and their WRs, which are close but not identical to those of Kidson (2000). They found non-linear changes in seasonal occurrence between El Niño and La Niña events in winter (May-September) over the period 1958-1996 (Jiang et al. 2004). Here, we re-investigate the relationship between Kidson types and ENSO, considering not only seasonal frequency of WRs but also the descriptors of their atmospheric centers of action.

Figure 8 shows the teleconnection with global SST fields for the winter season, using again the case of regime TNW (Fig. 3) as an example of a regime strongly associated with large-scale climate variability (Figs. 6-7). SST is used as a proxy to detect the spatial signature of the main

modes of climate variability, especially at low latitudes. After linearly removing the variance associated with the synchronous mean Niño3.4 index, partial teleconnections (independent of ENSO variability) are used to separate the role of ENSO from signals independent of it (implying that correlations that are unchanged when removing the signals associated with ENSO are interpreted here as mostly independent from it). Wintertime occurrence of the TNW regime is significantly favored by cold conditions in the eastern Pacific and in the northwestern Indian Ocean; the latter is statistically independent of ENSO (as revealed by the partial teleconnection similar to the "total" correlations including ENSO variability). The strongest signals concern the longitude of both centers of action (*LonMin*, *LonMax*), with El Niño conditions associated with a westernmost location of the trough and ridge of regime TNW. The ridge location is also related to SST signals in the west and southwest Pacific that are statistically independent of ENSO, while similar but weaker relationships are also found between SST variability in these regions and the intensity of the atmospheric ridge ($Max_{Z'}$). Finally, many descriptors show significant associations with seasonal SST at finer spatial scales, in the South Pacific basin around ANZ. This is especially the case for the metrics monitoring the geopotential gradient associated with the TNW regime, namely $Diff_{Z'}$, $Diff_{Lon}$ and *Grad*.

Figure 6 generalizes these results for all descriptors of all 12 WRs in winter, and Figure 7 extends them to the austral summer season. In winter (Fig. 6), regime W is the only one showing significant associations with ENSO for seasonal occurrence. Overall, the influence of ENSO on the WRs is moderate during summer. It mostly modulates the longitude of atmospheric lows (regimes T and TNW) or highs (TNW), acting to shift them eastwards under El Niño conditions. The mid-latitudes east of ANZ have already been identified as a region where El Niño events (including El Niño Modoki: Ashok and Yamagata, 2009) weaken the storm track over the South

Pacific sector (Ashok et al. 2009). How such changes in the storm track relate to changes in the WRs needs to be assessed in future work, but is outside the scope of this study. El Niño conditions also act to shift the HSE regime southwards and to reduce the geopotential height gradients associated with regime R. Relationships strengthen in summer, when ENSO reaches its seasonal peak of variance (Fig. 7), for at least one WR. Regime W shows a particularly strong response to ENSO, with increased seasonal occurrence under El Niño conditions and more intense atmospheric ridges at higher latitudes, which enhances the geopotential gradient with corresponding troughs (see Supp. Fig. 13). For other WRs, the ENSO influence essentially consists of longitudinal (TNW, NE) or latitudinal (HW) shifts of centers of action, but these relationships are barely significant.

4.3 Relationships with the SAM

As WRs are related to mid-latitude dynamics, they could also be influenced by the high latitudes, and influence them in return (e.g., Thompson and Woodworth 2014). Indeed, the climate of the ANZ region is strongly influenced by the SAM (e.g., Ummenhofer and England 2007; Ummenhofer et al. 2009; Kidston et al. 2009; Thompson et al. 2011). Jiang *et al.* (2013b) found significant changes in occurrence of their synoptic WRs around ANZ, depending on the phase of the SAM. Here, we investigate how the SAM modulates not only WR occurrence, but also their centers of action.

Figure 9 shows the association between regime TNW and the 700 hPa geopotential height (widely used to depict the SAM; e.g., Pohl and Fauchereau 2012) in the Southern Hemisphere, at the interannual timescale and for the winter season. Around ANZ, the spatial signature of the TNW regime (Fig. 3) is discernible, indicating that increased WR occurrence leads to changes

in the seasonal mean Z700 field through cumulative effects and upscaling processes. This pattern of regional extension matches the daily anomalies associated with this regime at the synoptic scale (Fig. 3), albeit with a larger negative anomaly region spreading across Australia. Interannual changes in occurrence are only weakly related to Z700 over Antarctica, suggesting limited associations with the SAM (confirmed in Fig. 7). Strong hemispheric-scale signals are found for the spatial coordinates of the atmospheric ridge of regime TNW (Fig. 3): negative Z700' over Antarctica (and thus positive polarities of the SAM: Fig. 6) are associated with southernmost and, even more strongly, easternmost locations of the ridge associated with this regime. Other descriptors may be associated with zonally symmetric Z700' in the Southern Hemisphere, but these signals are much weaker and barely significant.

While Figure 9 shows the statistical relationships between regime TNW and the SAM at the interannual timescale, Figure 10 extends these results to the intraseasonal timescale. It presents the composite Z700' daily anomalies associated with regime TNW, including the opposite phases of its descriptors, represented at the hemispheric-scale to identify potential signals in remote regions (denoting, for instance, associations with the high-frequency fluctuations of the SAM over Antarctica). Regional-scale signals in the ANZ sector are very close to the composite Z1000' of Fig. 3, with changes in the location or intensity of the centers of action directly translating into marked changes in the Z700' patterns (Fig. 10). At broader scales, the atmospheric ridge associated with TNW, southeast of ANZ, is likely to merge with large-scale Z700' patterns extending over Antarctica. Particularly intense ridges or anomalous southern locations are favorable conditions for the geopotential height signals to form a continuous pattern extending over most of the polar region. This is due to the larger spatial coherence and extension of geopotential height variability in the high versus mid-latitudes, where the transient perturbations embedded in synoptic-scale disturbances and/or wave trains limit the extension

but generally enhance the magnitude of short-lived perturbations in the geopotential height (Pohl and Fauchereau 2012). Figure 10 also shows that, at intraseasonal timescales, the relationships of the WRs with the SAM and high latitudes are strongly asymmetric, since the opposite phases of the descriptors lead to contrasting, but not opposite, large-scale Z700'. This asymmetry concerns almost all descriptors of this regime (Fig. 10). This could impact on the teleconnection analysis when considering the interannual variability of TNW descriptors and their relationship to large-scale climate conditions (Figs. 8-10). For instance, interannual associations between the SAM and the latitude of atmospheric troughs are less significant over Antarctica than intraseasonal anomalies at daily timescale, but this is not the case for their longitude. A possible reason is the opposite sign of the intraseasonal variations in Z700 over parts of the polar region between the opposite phases of this descriptor, tending thus towards more linear relationships even at intraseasonal scales.

Figs. 6-7 extend the analysis of interannual co-variability between the SAM and WR descriptors, while Figs. 11-12 show the composite analysis of short-lived SAM changes in polarity during the opposite phases of all descriptors of all WRs. At the interannual timescale, there are significant associations between WR seasonal occurrence and the synchronous SAM index. Relationships tend to be stronger in winter. When significant, they mostly consist of negative correlations with “Low” regimes, positive correlations for “High” regimes or with the ridges of “Gradient” regimes. This also holds for internal descriptors. The properties (especially the latitudes) of atmospheric lows generally show negative associations with the SAM, while the reverse tends to prevail for ridges. Troughs tend to locate further south during the positive phase of the SAM, and the ridges further north. This is consistent with the recorded southward shift of the westerlies and storm tracks that coincided during the 20th century, with a trend towards positive polarity of the SAM. Yet, this result is only found here at the interannual

timescale, since most descriptors show non-significant long-term trends over the period 1979-2019. Noticeable exceptions are the latitude of atmospheric ridges (Section 4.1), for which low-frequency changes and interannual variability both depict a tendency for increased atmospheric stability at subtropical latitudes (Fahad et al. 2020). Such changes could have contributed to the persisting drought that recently occurred in the Cape Town area of South Africa between 2015 and 2017 (Pascale et al. 2020; Sousa et al. 2018; Burls et al. 2019), or parts of the North Island of ANZ (2018-2020). Such events are not unprecedented, especially for the region of Auckland (Fowler 1994), and had been mostly interpreted up to now as a remote consequence of ENSO (Fowler and Adams 2004). They could increase in severity and recurrence in the future, given the changing location of the storm track in climate change projections (e.g., Fahad *et al.*, 2020; Pascale *et al.*, 2020).

At the daily timescale, the spread of the violin plots in Figs. 11-12 (showing the statistical distribution of the daily SAM index during the opposite phases of all descriptors of all WRs) first indicates that the association between WRs and the state of the SAM is neither direct nor systematic. A wide range of SAM polarities can correspond to the opposite phases of all WR descriptors, even those previously identified as significantly related to large-scale geopotential anomalies in the southern high latitudes. This result is also true for the Kidson types themselves (Supp. Fig. 6), despite the well-documented relationships between WRs around ANZ and the SAM (Jiang et al. 2013a,b). In spite of large internal variability, there is strong co-variability between the SAM and the atmospheric centers of action. Relationships that are significant at the daily timescale are not always significant interannually. The most systematic relationship denotes the major influence of the SAM on the latitude of atmospheric ridges (in winter, for regimes TNW, H, HNW, HSE, HE, HW and R – shown in Fig. 11; in summer, for regimes H, HNW, W, HSE, HE, HW and R – shown in Fig. 12). The intensity of Z1000' associated with

650 such atmospheric ridges is also partly controlled by the SAM, and/or can influence the SAM variability in return (Thompson and Woodworth 2014). In winter, this result holds for regimes TNW, HE and R, and in summer, for TNW and W. Such association between atmospheric anomalies in the mid-latitudes and the polarity of the SAM could be especially relevant for the analysis of droughts in the southern mid-latitudes and subtropics (Pendergrass et al. 2020).

655

This section has shown that large-scale climate conditions show stronger association with WR intrinsic properties (especially, their main atmospheric centers of action) than their frequency. This is particularly meaningful, since internal diversity within WRs is only very rarely analyzed in the literature, and changes in WR frequency alone explain a limited fraction of climate

660 variability across time and spatial scales.

5. Discussion and conclusion

665 In this paper, we have introduced new descriptors that monitor the daily properties and variability of atmospheric centers of action (intensity and location of troughs and ridges, and the gradients between them, when applicable) associated with weather regimes (WRs). This methodology may be of major interest for regions where low-frequency climate variability and change modifies the internal properties of WRs, rather than their occurrence (e.g., Pohl et al.

670 2018; Champagne et al. 2019). This is, for instance, the case of the poleward expansion of the tropical circulation (Hu et al. 2011; Sousa et al. 2018) which is likely to modify the latitude of the storm tracks in the mid-latitudes of both hemispheres. The methodology has been tested here with synoptic WRs previously defined (Kidson, 2000; Fig. 1) in the Aotearoa New Zealand (ANZ) and Southwest Pacific sectors, but could be applied to most temperate and polar regions

where weather or atmospheric regimes and types are often based on geopotential height anomalies and variability. Statistically, some of the descriptors are not independent from the others (Supp. Tables 1-12), especially those monitoring the "gradients" of geopotential which are, by construction, derived from the metrics describing the opposite centers of action (e.g. ridges and troughs).

5.1 Implications for the ANZ region and climate

The weather regimes of Kidson (2000) have been routinely used for the analysis of the regional climate variability. Centers of action that drive atmospheric flow were found to be highly variable in both time and space domains for daily to interannual timescales (Figs. 4-5), and also in relation to low-frequency weather regime trends (Figs. 6-7). Atmospheric centers of action may strongly vary within a given season (meaning that two sequences or days of the same WR may occur with very dissimilar characteristics: Fig. 5). The reverse can also be found, so that specific WR behavior, in terms of weather system location or intensity, can persist for a whole season. This is because large-scale, low-frequency modes of climate variability in the Southern Hemisphere that conjointly operate at tropical and polar latitudes, simultaneously influence mid-latitude WRs (Figs. 6-7).

A potentially useful outcome of this study is the link found between modes of large-scale variability and the intrinsic properties of the weather regimes, especially their centers of action (Figs. 6-7). Such relationships can be, in some cases, much stronger than those involving regime occurrence, a result that could be especially meaningful for seamless forecasting exercises. Relationships of WRs with ENSO are of moderate magnitude and strongly season-dependent (Figs. 6-7-8). Even though ENSO seems to modulate the internal descriptors and associated

properties of Aotearoa New Zealand's WRs more strongly than WR occurrence, the robustness of these associations needs to be assessed over longer time periods, to determine if they could be used to improve seamless weather and climate predictions. Stronger relationships are identified between WR occurrence and properties of their atmospheric centers of action (especially ridges) in the mid-latitudes arising from variations in the SAM (Figs. 9-10). These results could be particularly meaningful given past and projected changes in the SAM and mid-latitude storm tracks in the Southern Hemisphere, under the combined influence of stratospheric ozone and ongoing climate change. Future work should also focus on other modes of variability and associated timescales that could not be considered in the present work, and their influence of WR occurrence and intrinsic features. This includes (multi-) decadal variability like that associated with the Pacific Decadal Oscillation (PDO) or the Interdecadal Pacific Oscillation (IPO; Lorrey et al. 2007), but also higher-frequency modes like the Baroclinic Annular Mode or the Madden-Julien Oscillation (Fauchereau et al. 2016).

The methodology developed here may also help improve analyses based on identification of past or recent analogues (e.g., Lorrey et al. 2007, 2008), by selecting more similar synoptic contexts, or by deliberately considering contrasted configurations related to modes of variability. This could lead to more refined detail of surface climate anomalies resulting from interactions between regional-scale atmospheric dynamics, thermodynamics, and local-scale topography. We plan to apply this framework to the climate of ANZ, by analyzing how atmospheric descriptors modulate temperature and precipitation anomaly patterns.

5.2 Methodological implications for the analysis of weather regimes and types

Monitoring the location and intensity of atmospheric centers of action is of major importance in understanding fluctuations and changes across weather to climate time frames in regions where horizontal transport and advection of mass, energy or momentum drive most climate variability. The usefulness and robustness of information related to these centers of action depend on their capability to influence nearby regions by controlling atmospheric fluxes that reach or transit over them. While tropical climate is mostly controlled by vertical profiles of temperature and humidity, which determine the stability of the air mass, most regions in the middle and high latitudes are under the direct influence of the alternation between atmospheric lows (troughs) and highs (ridges) that strongly modulate atmospheric fluxes, mostly through geostrophic winds. Hence, in these regions, atmospheric pressure or geopotential height are key variables or spatial fields to monitor. Although weather regime analysis provides a decisive step to identify the most robust and recurrent archetypes of such spatial fields, they lead to a too strong simplification and a discretization of variability patterns that are, in fact, complex and continuous in nature. The descriptors defined in this work help to overcome this limiting issue by extracting simple metrics (intensity and location of regional extremes of geopotential height anomalies) likely to modify climate variability patterns and daily weather maps over a whole region. Such descriptors are well suited for the extra-tropical climates, where the geostrophy is strong enough to interpret atmospheric circulation anomalies as a response to the horizontal gradients of pressure. The approach tested in this work over a temperate region of the Southern Hemisphere, could probably give satisfactory results in many parts of the world spanning from the sub-tropics to the poles.

The methodological advances proposed in this study complement classical WR analyses that commonly provide qualitative views of climate variability. WR internal descriptors allow multiple parts of a unique atmospheric configuration to be quantified, thereby addressing a

major limitation arising from simplification and reduction inherent in WRs on their own. We have also demonstrated that the quantitative definition of discrete weather types is a useful complementary component of k-means classification, since individual daily WRs vary so widely, but similar descriptors could equally complement the interpretation of the "nodes" obtained through self-organizing maps (SOMs). Conceptually, this approach makes advancements with more detailed quantification of physical properties for weather systems, which differs from "fuzzy" classifications that rely solely on statistical properties of spatial field characteristics accompanied by dissimilarity or distance metrics (e.g., Moron *et al.*, 2013; Moron and Robertson, 2020). These descriptors also allow qualitative regimes to better characterize continuous climate variability across a wide range of space and time scales.

By summarizing the most relevant information in the form of daily weather maps as simple time series, the descriptors strongly reduce the amount of data needed to monitor and infer daily or sub-daily climate variability over long periods. This makes this methodology well suited to analyzing changes in weather regimes across a wide range of timescales, including long-term changes either natural and anthropogenically forced. Longer reanalysis datasets covering the late 19th and the whole of the 20th centuries (Slivinski et al. 2019), as well as climate projections extending to 2100 (Eyring et al. 2016), will be analyzed using this approach in future research. This could help refine the analysis of climate change, and the way it could modify day-to-day weather at regional scales.

Acknowledgments

The authors thank the Journal of Climate editorial staff, and two anonymous reviewers whose constructive comments helped to improve this work. This study is a contribution to the International Research Programme VinAdapt funded by France and New Zealand, and sea4seas project funded by the University of Burgundy. AL and NF were supported by the NIWA Strategic Science Investment Fund project "Climate Present and Past". All analyses were made with Python (numpy, pandas, scipy, sklearn, math, matplotlib, cartopy, seaborn, and netCDF4), the developers of which are thanked. Calculations were performed using HPC resources from DNUM CCUB (Centre de Calcul de l'Université de Bourgogne).

References

Ackerley, D., and Coauthors, 2011: Using synoptic type analysis to understand New Zealand climate during the Mid-Holocene. *Clim. Past*, **7**, 1189–1207, doi:10.5194/cp-7-1189-2011.

Appelhans, T., A. Sturman, and P. Zawar-Reza, 2013: Synoptic and climatological controls of particulate matter pollution in a Southern Hemisphere coastal city. *Int. J. Climatol.*, **33**, 463–479, doi:10.1002/joc.3439.

Ashok, K., and T. Yamagata, 2009: The El Niño with a difference. *Nature*, **461**, 481–484, doi:10.1038/461481a.

——, C. Tam, and W. J. Lee, 2009: ENSO Modoki impact on the Southern Hemisphere storm track activity during extended austral winter. *Geophys. Res. Lett.*, **36**, L12705, doi:10.1029/2009GL038847.

Burls, N. J., R. C. Blamey, B. A. Cash, E. T. Swenson, A. al Fahad, M.-J. M. Bopape, D. M. Straus, and C. J. C. Reason, 2019: The Cape Town "Day Zero" drought and Hadley cell expansion. *npj Clim. Atmos. Sci.*, **2**, doi:10.1038/s41612-019-0084-6. http://dx.doi.org/10.1038/s41612-019-0084-6.

Cassou, C., 2008: Intraseasonal interaction between the Madden–Julian oscillation and the North Atlantic oscillation. *Nature*, **455**, 523–527, doi:10.1038/nature07286. http://www.nature.com/nature/journal/v455/n7212/abs/nature07286.html (Accessed September 17, 2013).

——, L. Terray, J. W. Hurrell, and C. Deser, 2004: North Atlantic Winter Climate Regimes: Spatial Asymmetry, Stationarity with Time, and Oceanic Forcing. *J. Clim.*, **17**, 1055–1068.

——, ——, and A. S. Phillips, 2005: Tropical Atlantic Influence on European Heat Waves. *J. Clim.*, **18**, 2805–2811.

Champagne, O., B. Pohl, S. McKenzie, J. F. Buoncristiani, E. Bernard, D. Joly, and F. Tolle, 2019: Atmospheric circulation modulates the spatial variability of temperature in the Atlantic–Arctic region. *Int. J. Climatol.*, **39**, 3619–3638, doi:10.1002/joc.6044.

Cheng, X., and J. M. Wallace, 1993: Cluster Analysis of the Northern Hemisphere Wintertime 500-hPa Height Field: Spatial Patterns. *J. Atmos. Sci.*, **50**, 2674–2696.

Christiansen, B., 2007: Atmospheric circulation regimes: Can cluster analysis provide the number? *J. Clim.*, **20**, 2229–2250, doi:10.1175/JCLI4107.1.

Coggins, J. H., S. Parsons, and D. Schiel, 2016: An assessment of the ocean wave climate of New Zealand as represented in Kidson's synoptic types. *Int. J. Climatol.*, **36**, 2481–2496, doi:10.1002/joc.4507.

Crétat, J., Y. Richard, B. Pohl, M. Rouault, C. Reason, and N. Fauchereau, 2012: Recurrent daily rainfall patterns over South Africa and associated dynamics during the core of the austral summer. *Int. J. Climatol.*, **32**, 261–273, doi:10.1002/joc.2266. http://doi.wiley.com/10.1002/joc.2266.

Eyring, V., S. Bony, G. A. Meehl, C. A. Senior, B. Stevens, R. J. Stouffer, and K. E. Taylor, 2016: Overview of the Coupled Model Intercomparison Project Phase 6 (CMIP6) experimental design and organization. *Geosci. Model Dev.*, **9**, 1937–1958, doi:10.5194/gmd-9-1937-2016.

Fahad, A. al, N. J. Burls, and Z. Strasberg, 2020: How will southern hemisphere subtropical anticyclones respond to global warming? Mechanisms and seasonality in CMIP5 and CMIP6 model projections. *Clim. Dyn.*, **55**, 703–718, doi:10.1007/s00382-020-05290-7. https://doi.org/10.1007/s00382-020-05290-7.

Fauchereau, N., B. Pohl, C. J. C. Reason, M. Rouault, and Y. Richard, 2009: Recurrent daily OLR patterns in the Southern Africa/Southwest Indian Ocean region, implications for South African rainfall and teleconnections. *Clim. Dyn.*, **32**, 575–591, doi:10.1007/s00382-008-0426-2. http://link.springer.com/10.1007/s00382-008-0426-2.

Fauchereau, N., B. Pohl, and A. Lorrey, 2016: Extratropical Impacts of the Madden–Julian Oscillation over New Zealand from a Weather Regime Perspective. *J. Clim.*, **29**, 2161–2175, doi:10.1175/JCLI-D-15-0152.1. http://journals.ametsoc.org/doi/10.1175/JCLI-D-15-0152.1.

Favier, V., and Coauthors, 2016: Atmospheric drying as the main driver of dramatic glacier wastage in the southern Indian Ocean. *Sci. Rep.*, **6**, 32396, doi:10.1038/srep32396. http://dx.doi.org/10.1038/srep32396.

Fogt, R. L., J. Perlwitz, A. J. Monaghan, D. H. Bromwich, J. M. Jones, and G. J. Marshall, 2009: Historical SAM Variability. Part II: Twentieth-Century Variability and Trends from Reconstructions, Observations, and the IPCC AR4 Models. *J. Clim.*, **22**, 5346–5365, doi:10.1175/2009JCLI2786.1. http://journals.ametsoc.org/doi/abs/10.1175/2009JCLI2786.1.

Fowler, A., 1994: Assessment of the Significance of the 1994 Drought in Auckland. *Weather Clim.*, **14**, 22–25.

Fowler, A., and K. Adams, 2004: Twentieth century droughts and wet periods in Auckland (New Zealand) and their relationship to ENSO. *Int. J. Climatol.*, **24**, 1947–1961, doi:10.1002/joc.1100.

Gibson, P. B., S. E. Perkins-Kirkpatrick, P. Uotila, A. S. Pepler, and L. V Alexander, 2017: On the use of self-organizing maps for studying climate extremes. *J. Geophys. Res.*, **122**, 3891–3903, doi:10.1002/2016JD026256.

Hersbach, H., and Coauthors, 2020: The ERA5 global reanalysis. *Q. J. R. Meteorol. Soc.*, **146**, 1999–2049, doi:10.1002/qj.3803.

Hewitson, B. C., and R. G. Crane, 2002: Self-organizing maps: Applications to synoptic climatology. *Clim. Res.*, **22**, 13–26, doi:10.3354/cr022013.

Hu, Y., C. Zhou, and J. Liu, 2011: Observational evidence for poleward expansion of the Hadley circulation. *Adv. Atmos. Sci.*, **28**, 33–44, doi:10.1007/s00376-010-0032-1.

Huang, B., and Coauthors, 2017: Extended reconstructed Sea surface temperature, Version 5 (ERSSTv5): Upgrades, validations, and intercomparisons. *J. Clim.*, **30**, 8179–8205, doi:10.1175/JCLI-D-16-0836.1.

Huth, R., 1996: An Intercomparison of Computer-Assisted Circulation Classification Methods. *Int. J. Climatol.*, **16**, 893–922, doi:10.1002/(SICI)1097-0088(199608)16:8<893::AID-JOC51>3.0.CO;2-Q. http://doi.wiley.com/10.1002/%28SICI%291097-0088%28199608%2916%3A8%3C893%3A%3AAID-JOC51%3E3.0.CO%3B2-Q.

Jiang, N., 2011: A new objective procedure for classifying New Zealand synoptic weather types during 1958-2008. *Int. J. Climatol.*, **31**, 863–879, doi:10.1002/joc.2126.

Jiang, N., J. Hay, and G. Fisher, 2004: Classification of New Zealand Synoptic Weather Types and Relation to the Southern Oscillation Index. *Weather Clim.*, **23**, 3–23, doi:10.2307/26169666.

Jiang, N., K. N. Dirks, and K. Luo, 2013a: Classification of synoptic weather types using the self-organising map and its application to climate and air quality data visualisation. *Weather Clim.*, **33**, 52–75, doi:10.2307/26169737.

——, G. Griffiths, and A. Lorrey, 2013b: Influence of large-scale climate modes on daily synoptic weather types over New Zealand. *Int. J. Climatol.*, **33**, 499–519, doi:10.1002/joc.3443.

Jones, J. M., R. L. Fogt, M. Widmann, G. J. Marshall, P. D. Jones, and M. Visbeck, 2009: Historical SAM Variability. Part I: Century-Length Seasonal Reconstructions. *J. Clim.*, 5319–5345, doi:10.1175/2009JCLI2785.1.

Kalnay, E., and Coauthors, 1996: The NCEP/NCAR 40-Year Reanalysis Project. *Bull. Am. Meteorol. Soc.*, **77**, 437–471. http://journals.ametsoc.org/doi/abs/10.1175/1520-0477(1996)077%3C0437:TNYRP%3E2.0.CO;2 (Accessed February 19, 2014).

Kidson, J. W., 2000: An Analysis of New Zealand synoptic types and their use in defining weather regimes. *Int. J. Climatol.*, **20**, 299–316.

Kidston, J., J. A. Renwick, and J. McGregor, 2009: Hemispheric-scale seasonality of the Southern Annular Mode and impacts on the climate of New Zealand. *J. Clim.*, **22**, 4759–4771, doi:10.1175/2009JCLI2640.1. http://journals.ametsoc.org/doi/abs/10.1175/2009JCLI2640.1 (Accessed September 17, 2013).

Lorrey, A., A. M. Fowler, and J. Salinger, 2007: Regional climate regime classification as a qualitative tool for interpreting multi-proxy palaeoclimate data spatial patterns: A New Zealand case study. *Palaeogeogr. Palaeoclimatol. Palaeoecol.*, **253**, 407–433, doi:10.1016/j.palaeo.2007.06.011.

——, P. Williams, J. Salinger, T. Martin, J. Palmer, A. Fowler, J.-X. Zhao, and H. Neil, 2008: Speleothem stable isotope records interpreted within a multi-proxy framework and implications for New Zealand palaeoclimate reconstruction. *Quat. Int.*, **187**, 52–75, doi:10.1016/j.quaint.2007.09.039.

——, and Coauthors, 2014: The Little Ice Age climate of New Zealand reconstructed from Southern Alps cirque glaciers: a synoptic type approach. *Clim. Dyn.*, **42**, 3039–3060, doi:10.1007/s00382-013-1876-8. http://link.springer.com/10.1007/s00382-013-1876-8 (Accessed June 13, 2014).

Lorrey, A. M., and N. C. Fauchereau, 2017: Southwest Pacific atmospheric weather regimes: linkages to ENSO and extra-tropical teleconnections. *Int. J. Climatol.*, doi:10.1002/joc.5304. http://doi.wiley.com/10.1002/joc.5304.

——, and Coauthors, 2012: Palaeocirculation across New Zealand during the last glacial maximum at ~21 ka. *Quat. Sci. Rev.*, **36**, 189–213, doi:10.1016/j.quascirev.2011.09.025. http://dx.doi.org/10.1016/j.quascirev.2011.09.025.

Lu, J., G. A. Vecchi, and T. Reichler, 2007: Expansion of the Hadley cell under global warming. *Geophys. Res. Lett.*, **34**, L06805, doi:10.1029/2006GL028443.

Marshall, G. J., 2003: Trends in the Southern Annular Mode from observations and reanalyses. *J. Clim.*, **16**, 4134–4143. http://journals.ametsoc.org/doi/abs/10.1175/1520-0442(2003)016%3C4134%3ATITSAM%3E2.0.CO%3B2 (Accessed September 17, 2013).

Michaelides, S. C., F. Liassidou, and C. N. Schizas, 2007: Synoptic Classification and Establishment of Analogues with Artificial Neural Networks. *Fog and Boundary Layer Clouds: Fog Visibility and Forecasting*, I. Gultepe, Ed., Basel, Birkhäuser Basel, 1347–1364.

Michelangeli, P.-A., R. Vautard, and B. Legras, 1995: Weather Regimes: Recurrence and Quasi Stationarity.pdf. *J. Atmos. Sci.*, **52**, 1237–1256.

Moron, V., and G. Plaut, 2003: The impact of El Niño-Southern Oscillation upon weather regimes over Europe and the North Atlantic during boreal winter. *Int. J. Climatol.*, **23**, 363–379, doi:10.1002/joc.890. http://doi.wiley.com/10.1002/joc.890 (Accessed October 13, 2013).

——, and A. W. Robertson, 2020: Tropical rainfall subseasonal-to-seasonal predictability types. *npj Clim. Atmos. Sci.*, **3**, doi:10.1038/s41612-020-0107-3. http://dx.doi.org/10.1038/s41612-020-0107-3.

——, P. Camberlin, and A. W. Robertson, 2013: Extracting subseasonal scenarios: An alternative method to analyze seasonal predictability of regional-scale tropical rainfall. *J. Clim.*, **26**, 2580–2600,

doi:10.1175/JCLI-D-12-00357.1.
——, A. W. Robertson, J. H. Qian, and M. Ghil, 2015: Weather types across the Maritime Continent: From the diurnal cycle to interannual variations. *Front. Environ. Sci.*, **2**, 1–19, doi:10.3389/fenvs.2014.00065.
——, B. Oueslati, B. Pohl, and S. Janicot, 2018: Daily weather types in February-June (1979-2016) and temperature variations in tropical North Africa. *J. Appl. Meteorol. Climatol.*, **57**, 1171–1195, doi:10.1175/JAMC-D-17-0105.1.
——, R. Barbero, J. P. Evans, S. Westra, and H. J. Fowler, 2019: Weather Types and Hourly to Multiday Rainfall Characteristics in Tropical Australia. *J. Clim.*, **32**, 3983–4011, doi:10.1175/JCLI-D-18-0384.1.
Nguyen, H., H. H. Hendon, E. P. Lim, G. Boschat, E. Maloney, and B. Timbal, 2018: Variability of the extent of the Hadley circulation in the southern hemisphere: a regional perspective. *Clim. Dyn.*, **50**, 129–142, doi:10.1007/s00382-017-3592-2.
Osman, M., B. Zaitchik, H. Badr, and S. Hameed, 2020: North Atlantic centers of action and seasonal to subseasonal temperature variability in Europe and eastern North America. *Int. J. Climatol.*, 1–16, doi:10.1002/joc.6806.
Ouzeau, G., J. Cattiaux, H. Douville, A. Ribes, and D. Saint-Martin, 2011: European cold winter 2009-2010: How unusual in the instrumental record and how reproducible in the ARPEGE-Climat model? *Geophys. Res. Lett.*, **38**, n/a--n/a, doi:10.1029/2011GL047667. http://doi.wiley.com/10.1029/2011GL047667 (Accessed September 17, 2013).
Parsons, S., A. J. McDonald, and J. A. Renwick, 2014: The use of synoptic climatology with general circulation model output over New Zealand. *Int. J. Climatol.*, **34**, 3426–3439, doi:10.1002/joc.3919.
Pascale, S., S. B. Kapnick, T. L. Delworth, and W. F. Cooke, 2020: Increasing risk of another Cape Town " Day Zero " drought in the 21st century. *Proc. Natl. Acad. Sci.*, 1–9, doi:10.1073/pnas.2009144117.
Pendergrass, A. G., and Coauthors, 2020: Flash droughts present a new challenge for subseasonal-to-seasonal prediction. *Nat. Clim. Chang.*, **10**, 191–199, doi:10.1038/s41558-020-0709-0. https://doi.org/10.1038/s41558-020-0709-0.
Perlwitz, J., 2011: Tug of war on the jet stream. *Nat. Clim. Chang.*, **1**, 29–31, doi:10.1038/nclimate1065. http://dx.doi.org/10.1038/nclimate1065.
Pohl, B., and N. Fauchereau, 2012: The Southern Annular Mode Seen through Weather Regimes. *J. Clim.*, **25**, 3336–3354, doi:10.1175/JCLI-D-11-00160.1. http://journals.ametsoc.org/doi/abs/10.1175/JCLI-D-11-00160.1.
——, B. Dieppois, J. Crétat, D. Lawler, and M. Rouault, 2018: From Synoptic to Interdecadal Variability in Southern African Rainfall : Toward a Unified View across Time Scales. *J. Clim.*, **31**, 5845–5872, doi:10.1175/JCLI-D-17-0405.1.
Polvani, L. M., D. W. Waugh, G. J. P. Correa, and S.-W. Son, 2011: Stratospheric Ozone Depletion: The Main Driver of Twentieth-Century Atmospheric Circulation Changes in the Southern Hemisphere. *J. Clim.*, **24**, 795–812, doi:10.1175/2010JCLI3772.1.
Rayner, N. A., D. E. Parker, E. B. Horton, C. K. Folland, L. V Alexander, D. P. Rowell, E. C. Kent, and A. Kaplan, 2003: Global analyses of sea surface temperature , sea ice, and night marine air temperature since the late nineteenth century. *J. Geophys. Res.*, **108**, 4407, doi:10.1029/2002JD002670.
Renwick, J. A., 2004: Trends in the Southern Hemisphere polar vortex in NCEP and ECMWF reanalyses. *Geophys. Res. Lett.*, **31**, L07209, doi:10.1029/2003GL019302.
Renwick, J. A., 2011: Kidson's Synoptic Weather Types and Surface Climate Variability over New Zealand. *Weather Clim.*, **31**, 3–23, doi:10.2307/26169715.
Richard, Y., and Coauthors, 2018: Urban Climate How relevant are local climate zones and urban climate zones for urban climate research ? Dijon (France) as a case study. *Urban Clim.*, **26**, 258–274, doi:10.1016/j.uclim.2018.10.002. https://doi.org/10.1016/j.uclim.2018.10.002.
Salinger, M. J., and Coauthors, 2020: Unparalleled coupled ocean-atmosphere summer heatwaves in the New Zealand region: drivers, mechanisms and impacts. *Clim. Change*, **162**, 485–506, doi:10.1007/s10584-020-02730-5.
Sheridan, S. C., and C. C. Lee, 2011: The self-organizing map in synoptic climatological research. *Prog. Phys. Geogr.*, **35**, 109–119, doi:10.1177/0309133310397582.
Slivinski, L. C., and Coauthors, 2019: Towards a more reliable historical reanalysis: Improvements for version 3 of the Twentieth Century Reanalysis system. *Q. J. R. Meteorol. Soc.*, **145**, 2876–2908, doi:10.1002/qj.3598.
Sousa, P. M., R. C. Blamey, C. J. C. Reason, A. M. Ramos, and R. M. Trigo, 2018: The "Day Zero" Cape Town drought and the poleward migration of moisture corridors. *Environ. Res. Lett.*, **13**, 124025, doi:10.1088/1748-9326/aaebc7.
Stephenson, D. B., A. Hannachi, and A. O'Niell, 2004: On the existence of multiple climate regimes. *Q. J. R. Meteorol. Soc.*, **130**, 583–605, doi:10.1256/qj.02.146.
Straus, D. M., S. Corti, and F. Molteni, 2007: Circulation regimes: Chaotic variability versus SST-forced

predictability. *J. Clim.*, **20**, 2251–2272, doi:10.1175/JCLI4070.1.
Tao, L., Y. Hu, and J. Liu, 2016: Anthropogenic forcing on the Hadley circulation in CMIP5 simulations. *Clim. Dyn.*, **46**, 3337–3350, doi:10.1007/s00382-015-2772-1.
Thompson, D. W. J., and J. D. Woodworth, 2014: Barotropic and baroclinic annular variability in the Southern Hemisphere. *J. Atmos. Sci.*, **71**, 1480–1493, doi:10.1175/JAS-D-13-0185.1.
——, S. Solomon, P. J. Kushner, M. H. England, K. M. Grise, and D. J. Karoly, 2011: Signatures of the Antarctic ozone hole in Southern Hemisphere surface climate change. *Nat. Geosci*, **4**, 741–749. http://dx.doi.org/10.1038/ngeo1296.
Ullmann, A., B. Fontaine, and P. Roucou, 2013: Euro-Atlantic weather regimes and Mediterranean rainfall patterns: present-day variability and expected changes under CMIP5 projections. *Int. J. Climatol.*, n/a--n/a, doi:10.1002/joc.3864. http://doi.wiley.com/10.1002/joc.3864 (Accessed January 30, 2014).
Ummenhofer, C. C., and M. H. England, 2007: Interannual extremes in New Zealand precipitation linked to modes of Southern Hemisphere climate variability. *J. Clim.*, **20**, 5418–5440, doi:10.1175/2007JCLI1430.1.
——, A. Sen Gupta, and M. H. England, 2009: Causes of late twentieth-century trends in New Zealand precipitation. *J. Clim.*, **22**, 3–19, doi:10.1175/2008JCLI2323.1.
Vautard, R., 1990: Multiple Weather Regimes over the North Atlantic: Analysis of Precursors and Successors. *Mon. Weather Rev.*, **118**, 2056–2081. http://journals.ametsoc.org/doi/abs/10.1175/1520-0493(1990)118%3C2056:MWROTN%3E2.0.CO;2 (Accessed October 23, 2013).
Vigaud, N., and A. Robertson, 2017: Convection regimes and tropical-midlatitude interactions over the Intra-American Seas from May to November. *Int. J. Climatol.*, doi:10.1002/joc.5051. http://doi.wiley.com/10.1002/joc.5051.
——, B. Pohl, and J. Crétat, 2012: Tropical-temperate interactions over southern Africa simulated by a regional climate model. *Clim. Dyn.*, **39**, 2895–2916, doi:10.1007/s00382-012-1314-3.
Vrac, M., P. Vaittinada Ayar, and P. Yiou, 2014: Trends and variability of seasonal weather regimes. *Int. J. Climatol.*, **34**, 472–480, doi:10.1002/joc.3700.
Zheng, F., J. Li, R. T. Clark, and H. C. Nnamchi, 2013: Simulation and projection of the Southern Hemisphere annular mode in CMIP5 models. *J. Clim.*, **26**, 9860–9879, doi:10.1175/JCLI-D-13-00204.1.

Figures & Tables

	Low (Trough)			High (Ridge)			Gradient (Trough and Ridge)			
	Lat	Lon	$Min_{Z'}$	Lat	Lon	$Max_{Z'}$	$Diff_{Lat}$	$Diff_{Lon}$	$Diff_{Z'}$	Grad
T	x	x	x							
SW	x	x	x							
TNW	x	x	x	x	x	x	x	x	x	x
TSW	x	x	x							
H				x	x	x				
HNW	x	x	x	x	x	x	x	x	x	x
W	x	x	x	x	x	x	x	x	x	x
HSE				x	x	x				
HE	x	x	x	x	x	x	x	x	x	x
NE	x	x	x	x	x	x	x	x	x	x
HW	x	x	x	x	x	x	x	x	x	x
R	x	x	x	x	x	x	x	x	x	x

Table 1. Overview of the internal descriptors used for each of the 12 KTs (in rows). "Low" columns are for troughs, "High" columns for ridges, and "Gradient" columns for regimes showing both troughs and ridges. Internal descriptors depict the spatial coordinates (*Lat*, *Lon*) and intensities ($Min_{Z'}$, $Max_{Z'}$) of centres of action, and for gradient types, their differences ($Diff_{Lat}$, $Diff_{Lon}$, $Diff_{Z'}$). *Grad* corresponds to the geopotential height gradient between both centres of action. See text for further details.

			NCEP/NCAR											
			T	**SW**	**TNW**	**TSW**	**H**	**HNW**	**W**	**HSE**	**HE**	**NE**	**HW**	**R**
			1741	**1774**	**1042**	**837**	**2105**	**1177**	**830**	**2017**	**1143**	**801**	**828**	**670**
ERA-5	**T**	**1633**	***1167***	239	113	74	0	0	39	0	0	0	0	1
	SW	**1281**	118	***1000***	5	31	0	72	34	0	0	0	16	5
	TNW	**983**	158	3	***660***	33	0	0	16	0	34	59	0	20
	TSW	**867**	144	95	50	***533***	0	0	0	0	0	18	9	18
	H	**1580**	0	0	0	0	***1259***	121	3	115	45	0	36	1
	HNW	**1249**	6	149	2	0	228	***714***	73	4	7	0	57	9
	W	**1294**	127	142	61	3	60	147	***611***	3	122	2	3	13
	HSE	**1913**	0	0	0	0	246	0	0	***1465***	82	27	60	33
	HE	**1232**	4	2	30	1	157	9	40	162	***768***	29	8	22
	NE	**904**	3	2	77	51	1	0	1	52	52	***617***	12	36
	HW	**1189**	5	113	1	28	148	110	4	138	5	14	***584***	39
	R	**840**	9	29	43	83	6	4	9	78	28	35	43	***473***

Table 2. Contingency table showing the agreements and disagreements between the NCEP/NCAR original distribution of KTs and their redefinition with ERA5 classification. For each reanalysis, the cluster size is given (in bold). The diagonal cells (bold italics) denote agreement of KTs between both reanalyses.

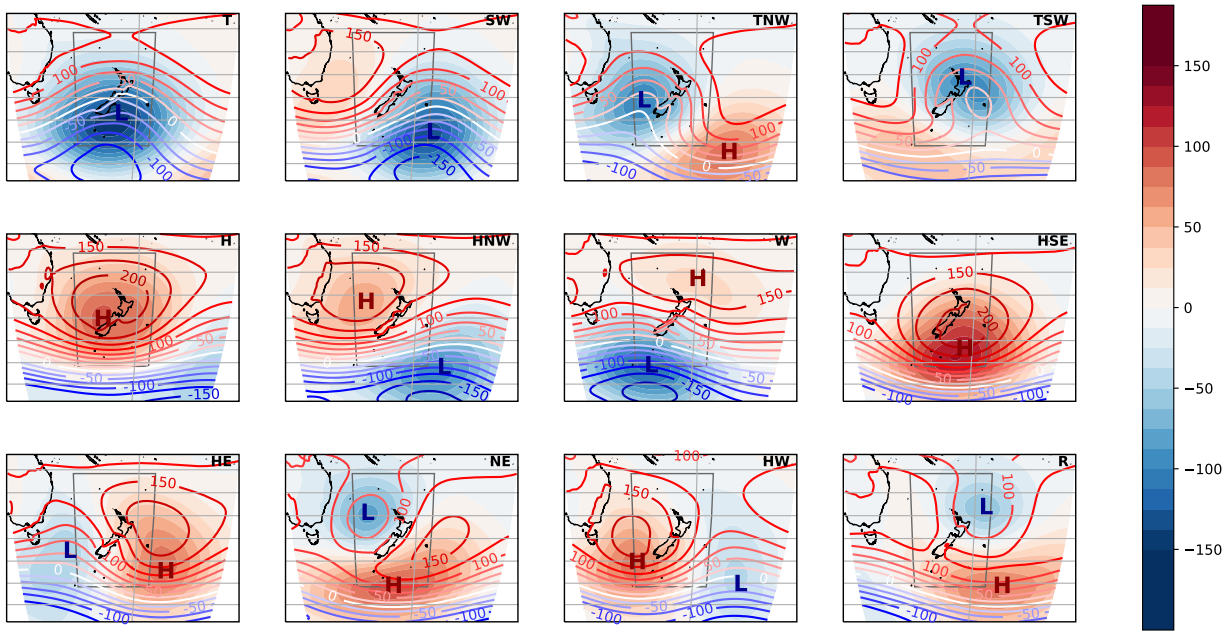

Figure 1. Contours of composite geopotential height at 1000 hPa associated with the 12 weather regimes of Kidson (2000). Color shading corresponds to Z1000 anomalies. Only anomalies that are statistically different from the climatology according to a one-tailed t-test at the 95% level are represented. The inner rectangle represents the domain used by Kidson (2000). H: local maximum Z1000 anomalies. L: local minimum Z1000 anomalies. Geopotential height derived from ERA-5 reanalysis, period 1979-2019.

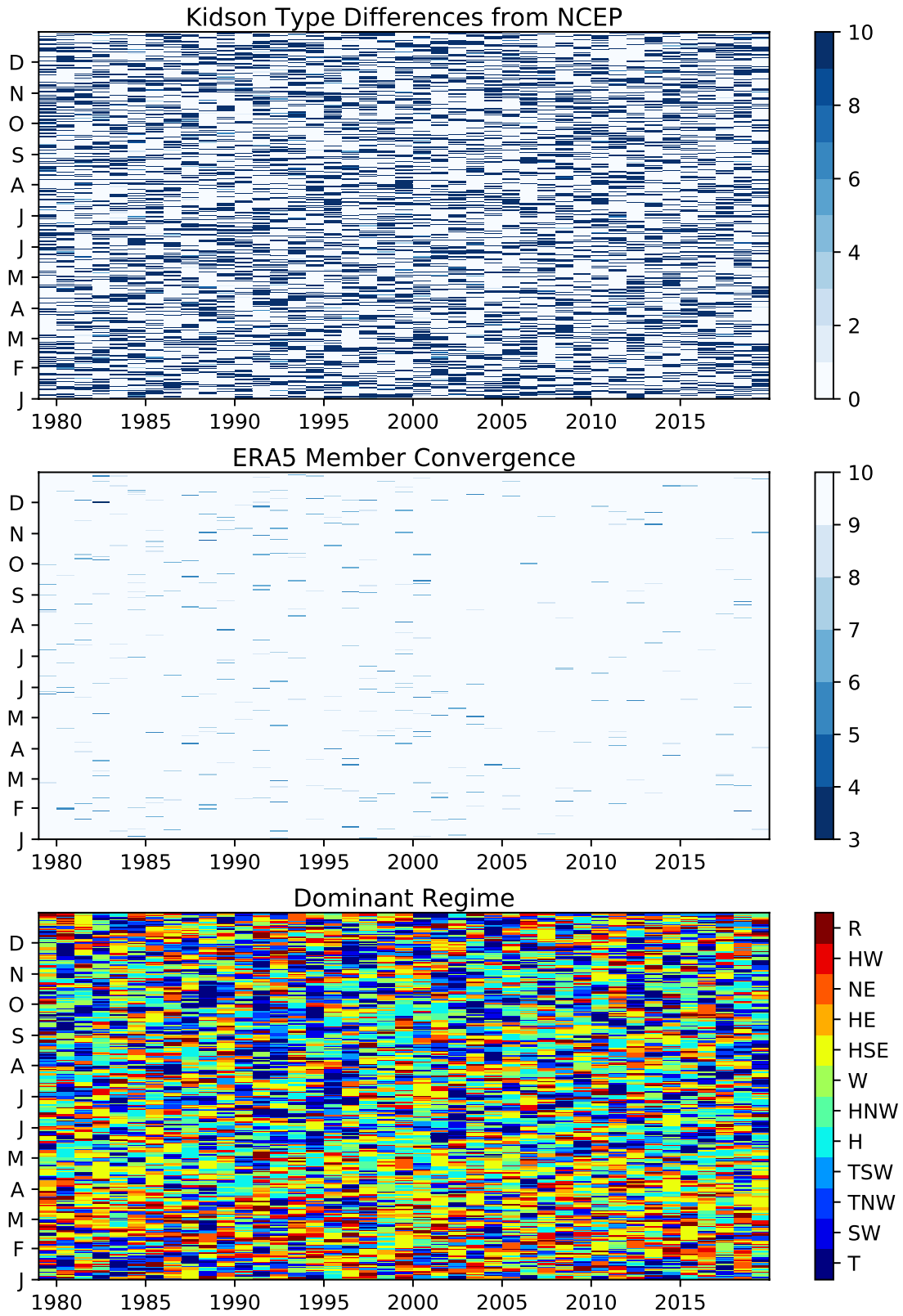

Figure 2. Kidson type dependency on ERA5 versus NCEP/NCAR reanalysis. Upper panel: disagreement between the type classification inherited from NCEP/NCAR and that redefined using ERA5. Middle panel: ensemble reproducibility in ERA5 (for each day, the number of members ascribed to the same type, out of 10 ensemble members). Lower panel: the dominant Kidson Type (KT) in the ERA5 ensemble for each day of the period 1979-2019.

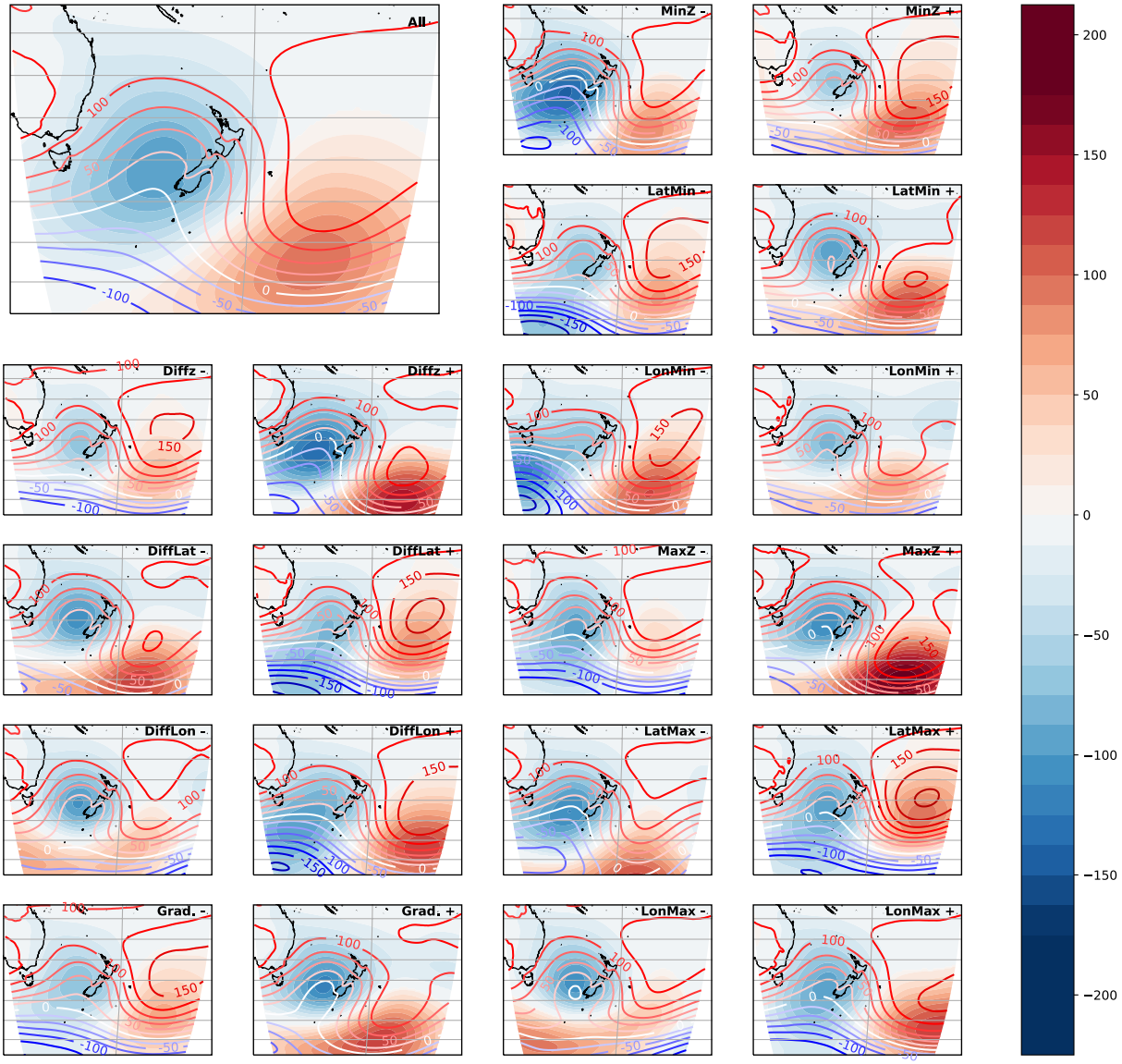

Figure 3. Z1000 raw fields (contours) and Z1000' anomalies (color shading) during the TNW type. All: all occurrences of TNW. For each of the internal descriptors of Table 1, the – and + maps show the 20% weakest and 20% strongest values of the distribution of the corresponding descriptor. Common days between samples of different descriptors are counted in Supp. Table 1. For all maps, only anomalies that are statistically different from the climatology according to a one-tailed t-test at the 95% level are represented.

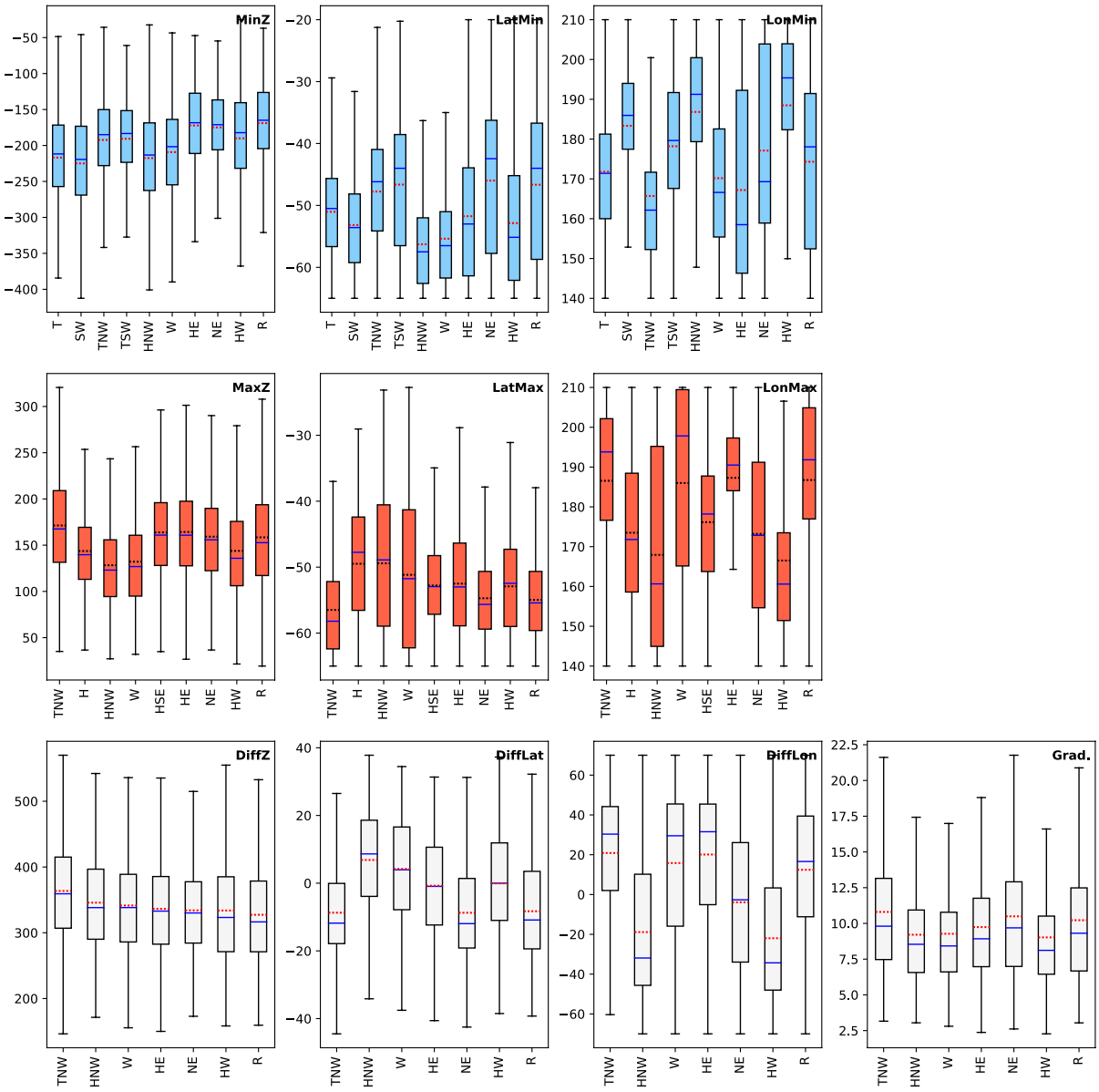

Figure 4. Box-and-whisker representation of the statistical distribution of each descriptor (blue: Low types; red: High types; white: Gradient types) according to the ERA5 ensemble mean. The boxes have lines at the lower quartile, median (blue line) and upper quartile values. The average is shown by the dashed red lines. The whiskers are lines extending from each end of the box up to the 1.5 interquartile range. Outliers have been omitted for readability.

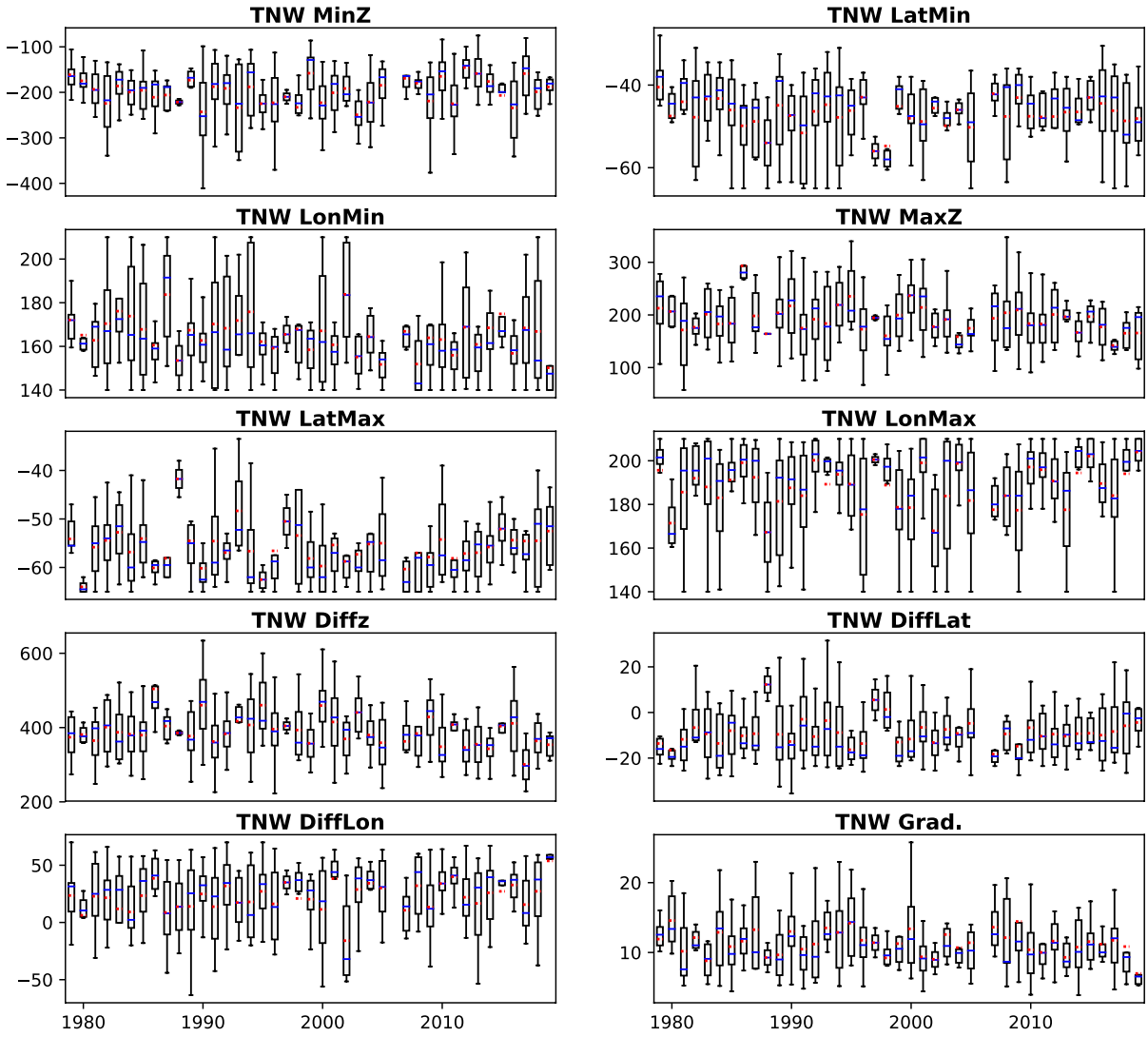

Figure 5. Box-and-whisker representation of the intraseasonal (shown by the range of each box-and-whisker) versus interannual (shown by the differences between boxes and whiskers) statistical distributions of the daily descriptors of the TNW type for the austral winter season, period JJAS 1979-2019. Representation as for Fig. 4.

		Count	Low			High			Gradient			
			$Min_{Z'}$	Lat	Lon	$Max_{Z'}$	Lat	Lon	$Diff_{Z'}$	$Diff_{Lat}$	$Diff_{Lon}$	Grad
T	SAM	-0.35	0.05	-0.39	0.01							
	ENSO	0.03	0.22	0.15	0.30							
SW	SAM	-0.27	-0.07	-0.31	-0.24							
	ENSO	0.13	-0.18	0.01	0.21							
TNW	SAM	-0.24	0.03	-0.01	0.18	-0.00	0.24	0.56	-0.02	0.17	0.32	-0.04
	ENSO	-0.25	-0.13	-0.07	0.47	0.04	-0.00	0.38	0.12	0.04	-0.01	0.15
TSW	SAM	-0.21	0.07	-0.30	-0.15							
	ENSO	-0.01	-0.22	-0.27	-0.15							
H	SAM	0.44				-0.10	0.10	0.11				
	ENSO	-0.02				0.18	-0.18	0.19				
HNW	SAM	0.17	0.17	0.03	-0.07	-0.18	0.20	0.04	-0.24	0.14	0.06	-0.01
	ENSO	0.16	0.03	0.18	-0.06	0.00	-0.14	0.19	-0.02	-0.17	0.16	0.15
W	SAM	-0.19	-0.10	-0.27	0.15	0.03	0.13	0.12	0.11	0.23	-0.01	0.15
	ENSO	0.32	0.01	0.01	0.08	0.02	-0.10	0.14	0.00	-0.08	0.05	0.15
HSE	SAM	0.01				-0.19	0.24	0.16				
	ENSO	-0.19				0.12	-0.31	-0.20				
HE	SAM	0.43	0.12	-0.49	-0.12	-0.07	0.42	0.35	-0.15	0.52	0.33	-0.37
	ENSO	0.07	-0.06	-0.06	-0.01	-0.09	-0.07	0.01	-0.01	0.01	0.02	-0.31
NE	SAM	-0.22	0.15	-0.13	-0.08	-0.02	0.27	0.19	-0.11	0.23	0.18	-0.19
	ENSO	-0.29	-0.04	0.16	-0.02	0.18	-0.17	-0.02	0.15	-0.20	-0.00	-0.12
HW	SAM	0.14	0.07	-0.10	-0.25	-0.08	0.45	-0.03	-0.09	0.44	0.10	-0.14
	ENSO	-0.11	-0.15	0.10	0.11	0.18	0.09	-0.10	0.21	-0.01	-0.13	-0.02
R	SAM	0.27	0.05	-0.35	-0.07	-0.27	0.46	-0.01	-0.23	0.47	0.03	-0.35
	ENSO	0.06	0.05	-0.04	-0.23	-0.12	-0.02	0.11	-0.12	-0.04	0.21	-0.38

Figure 6. Correlations between austral winter season regime occurrence ("count") and their seasonal mean internal descriptors with the synchronous SAM and Niño3.4 (ENSO) seasonal mean indices, for the period JJAS 1979-2019. Values in blue (red) are negative (positive) correlations that are statistically significant at the 95% level according to a Bravais-Pearson test. Table cells with background blue (red) colours indicate 95% significant negative (positive) long-term trends over the period 1979-2019 according to Spearman's rank correlation test.

1070

		Count	Low			High			Gradient			
			$Min_{Z'}$	Lat	Lon	$Max_{Z'}$	Lat	Lon	$Diff_{Z'}$	$Diff_{Lat}$	$Diff_{Lon}$	Grad
T	SAM	-0.51	0.02	0.24	-0.17							
	ENSO	0.09	-0.09	-0.25	0.09							
SW	SAM	-0.41	0.13	-0.30	-0.16							
	ENSO	0.47	-0.31	-0.18	0.17							
TNW	SAM	0.07	0.18	-0.13	-0.30	-0.28	0.30	0.15	-0.13	0.26	0.28	-0.27
	ENSO	-0.15	-0.22	0.02	0.31	0.03	-0.08	-0.26	0.17	-0.06	-0.36	0.17
TSW	SAM	0.26	-0.02	-0.18	0.24							
	ENSO	-0.27	0.08	0.14	0.07							
H	SAM	0.26				-0.18	0.28	-0.00				
	ENSO	0.16				0.00	-0.06	0.13				
HNW	SAM	-0.19	-0.14	-0.32	0.04	0.16	-0.08	-0.23	0.24	0.13	-0.19	-0.08
	ENSO	0.29	0.10	-0.16	-0.03	-0.25	0.11	0.02	-0.24	0.17	0.03	-0.04
W	SAM	-0.20	0.04	-0.18	-0.01	-0.05	0.24	-0.18	-0.07	0.28	-0.13	-0.23
	ENSO	0.46	-0.14	-0.11	-0.04	0.46	-0.31	0.27	0.43	-0.22	0.18	-0.02
HSE	SAM	-0.20				0.11	0.02	0.02				
	ENSO	-0.42				-0.15	-0.04	0.24				
HE	SAM	0.31	-0.04	-0.09	-0.19	-0.05	0.19	0.12	-0.01	0.16	0.21	-0.15
	ENSO	-0.05	0.04	0.16	-0.14	0.18	-0.06	-0.06	0.14	-0.13	0.08	0.07
NE	SAM	0.10	-0.06	-0.15	-0.23	-0.32	0.36	0.27	-0.19	0.28	0.31	-0.22
	ENSO	-0.19	0.02	0.04	-0.07	0.22	-0.19	-0.30	0.14	-0.12	-0.13	0.14
HW	SAM	0.39	0.16	-0.21	-0.12	0.02	0.24	-0.07	-0.14	0.30	0.04	-0.04
	ENSO	-0.16	0.02	0.30	-0.02	-0.03	0.06	0.23	-0.05	-0.18	0.13	0.27
R	SAM	-0.18	-0.28	-0.02	0.16	-0.33	0.07	-0.07	-0.00	-0.07	-0.14	-0.04
	ENSO	0.02	0.18	-0.09	-0.02	0.33	-0.04	-0.09	0.09	-0.12	-0.04	0.02

Figure 7. As Figure 6, but for the austral summer season (NDJF 1979-80 to 2018-19).

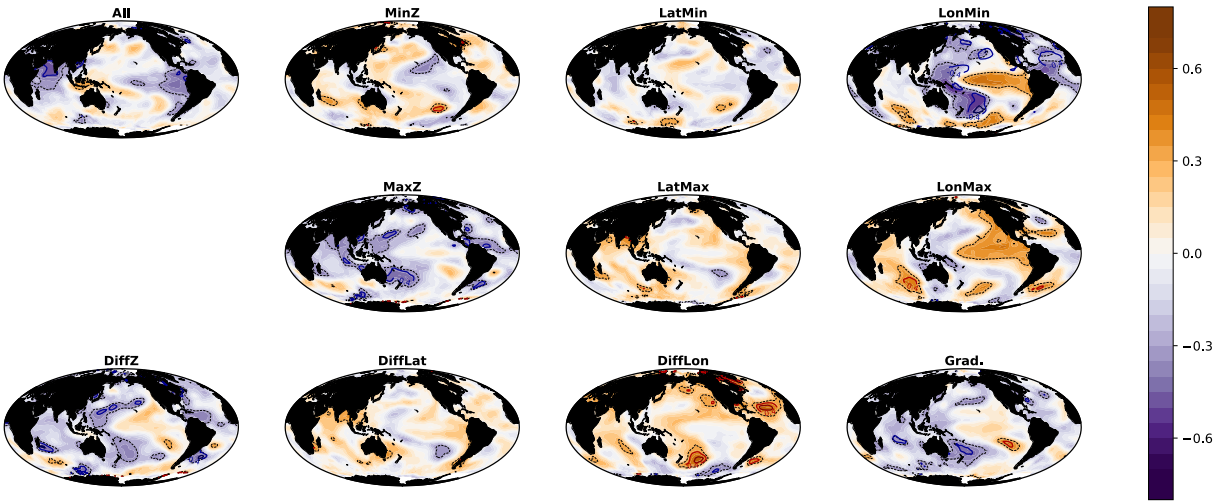

Figure 8. Correlations between the seasonal mean SST and the seasonal mean occurrence ("All") of the TNW type and each of its internal descriptors, JJAS 1979-2019. Colours represent linear correlations, with the dashed lines indicating 95% significance according to a Bravais-Pearson test. The solid contours represent partial positive (in red) and negative (in blue) correlations after removing the variance associated with the seasonal mean Niño3.4 index. Only significant partial correlations according to a Bravais-Pearson test at the 95% level are displayed.

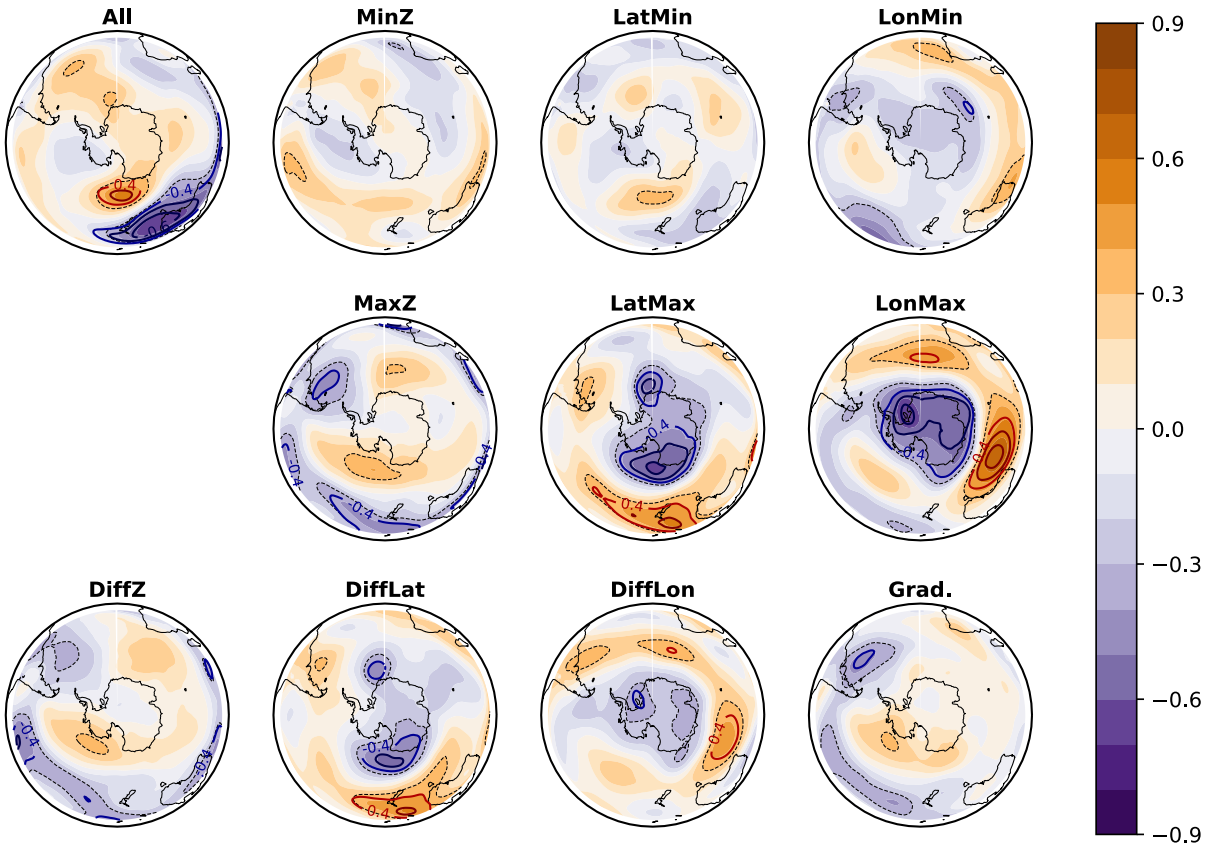

Figure 9. Correlations between seasonal mean Z700 field and the seasonal mean occurrence ("All") of the TNW type and each of its internal descriptors, JJAS 1979-2019. Colours represent linear correlations, with the dashed lines indicating 95% significance according to a Bravais-Pearson test. The solid contours represent partial positive (in red) and negative (in blue) correlations after removing the variance associated with the seasonal mean SAM index of Marshall (2003) index. Only significant partial correlations according to a Bravais-Pearson test at the 95% level are displayed.

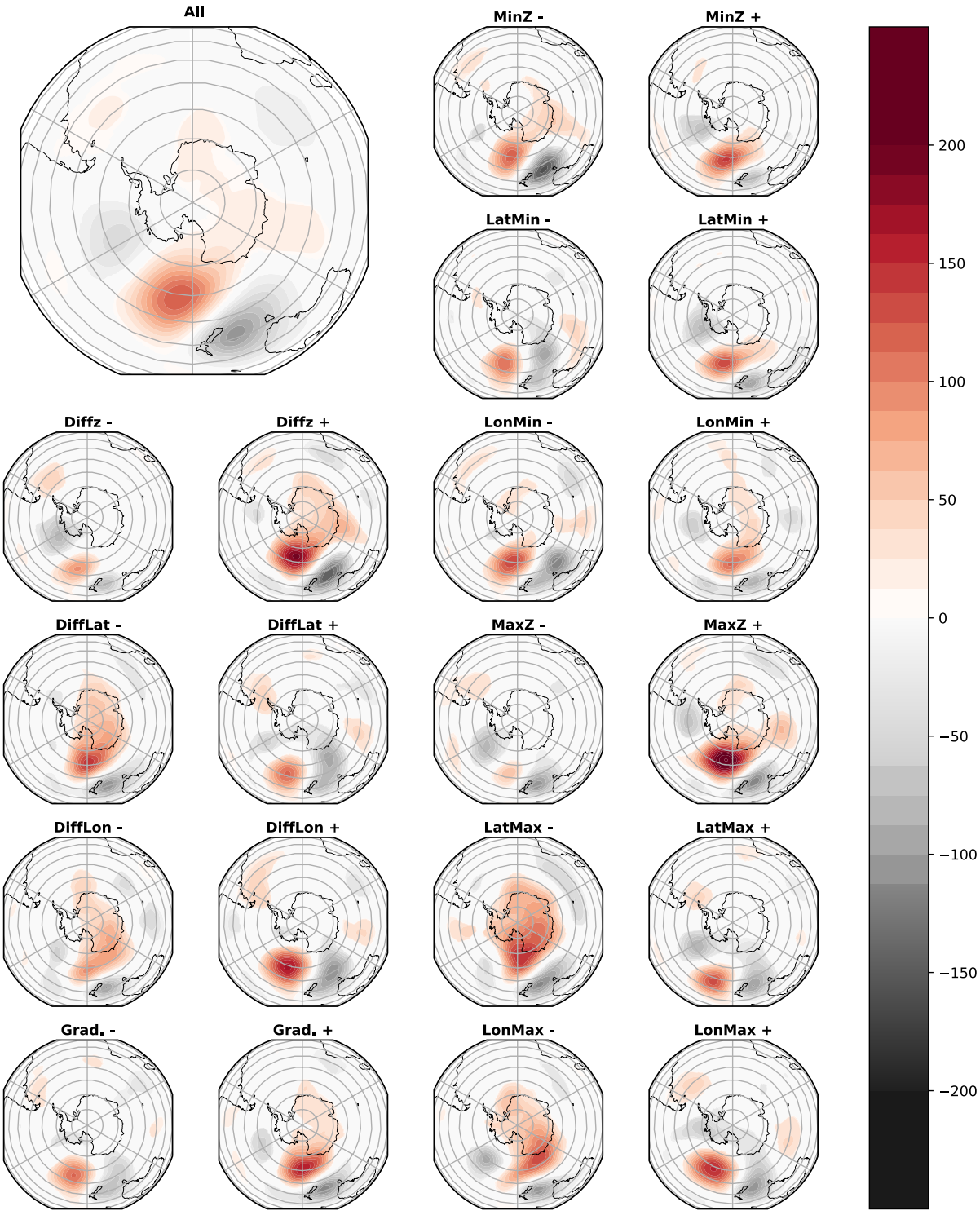

Figure 10. Composite anomalies of daily Z700 anomalies during the occurrence of the TNW type, for all occurrences ("All") and the opposite phases (below the 20th and above the 80th percentiles) of each of its internal descriptors, over the period JJAS 1979-2019. For all maps, only anomalies that are statistically different from the climatology according to a one-tailed t-test at the 95% level are represented.

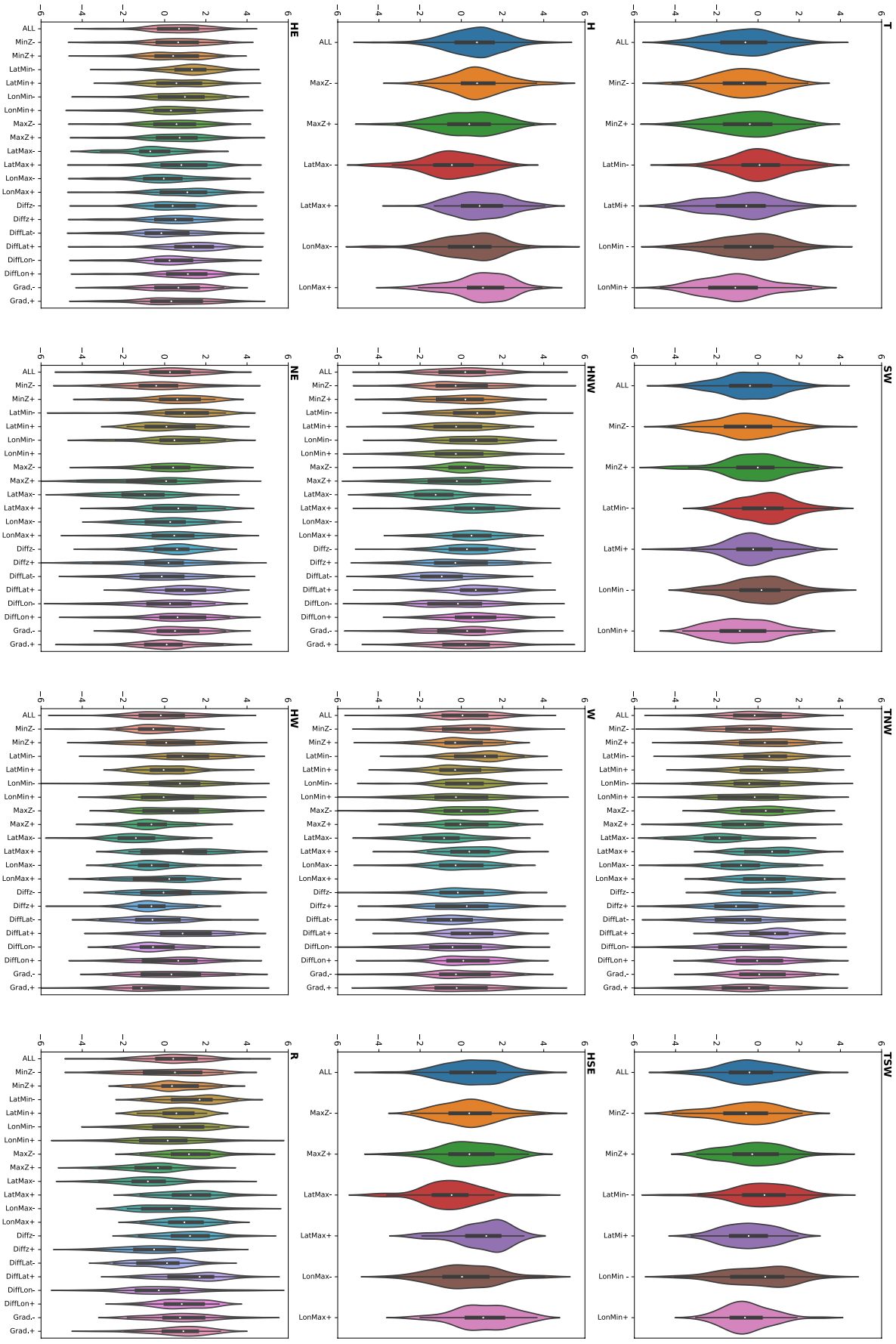
T
H
HE
SW
HNW
NE
TNW
W
HW
TSW
HSE
R
ALL
MinZ-
MinZ+
LatMin-
LatMin+
LonMin-
LonMin+
MaxZ-
MaxZ+
LatMax-
LatMax+
LonMax-
LonMax+
Diffz-
Diffz+
DiffLat-
DiffLat+
DiffLon-
DiffLon+
Grad.-
Grad.+

1105

← **Figure 11.** Violin plots representing variation of the daily SAM index of Marshall (2003) for the austral winter season during the occurrence of each Kidson type, for all occurrences ("All") and the opposite phases (below the 20th and above the 80th percentiles) of each of their internal descriptors. The boxes extend between the lower and upper quartile values, and the median is shown by white dots. The violins show smoothed statistical distributions of the daily SAM index, as estimated by smoothed kernel density estimations, for the opposite phases of each daily descriptor, and over the period JJAS 1979-2019.

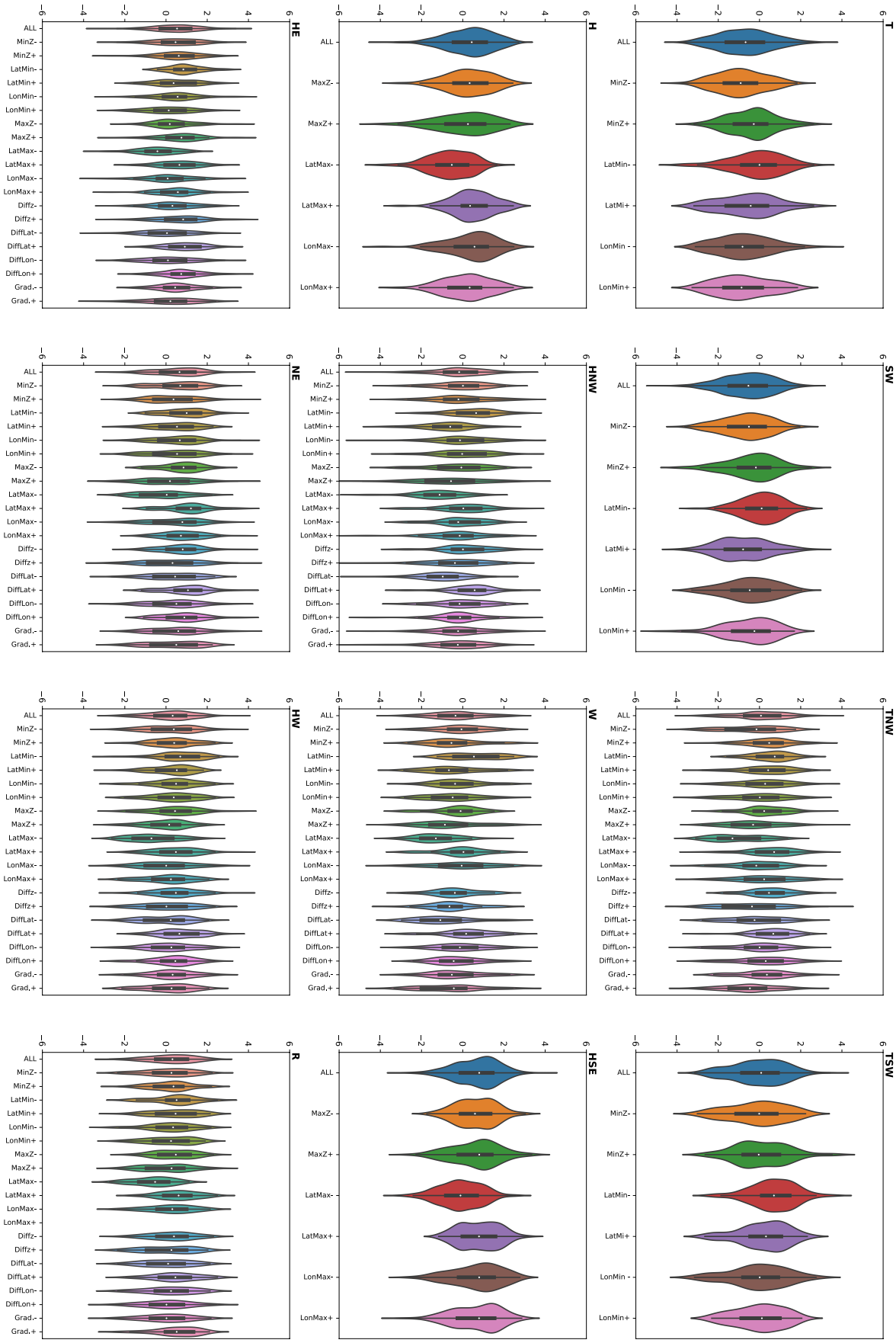

1115

Figure 12. As Figure 11, but for the austral summer season (NDJF 1979-80 to 2018-19).